NAVAL POSTGRADUATE SCHOOL
Monterey, California

THESIS

THE INFLUENCE OF SHALLOW WATER VARIABILITY ON SHORT RANGE WATER-BOURNE PROPAGATION

by

Stephen C. Karpi

December 2002

Thesis Advisor:	Kevin B. Smith
Thesis Co-Advisor:	Peter H. Dahl

Approved for public release; distribution is unlimited.

THIS PAGE INTENTIONALLY LEFT BLANK

REPORT DOCUMENTATION PAGE			*Form Approved OMB No. 0704-0188*
Public reporting burden for this collection of information is estimated to average 1 hour per response, including the time for reviewing instruction, searching existing data sources, gathering and maintaining the data needed, and completing and reviewing the collection of information. Send comments regarding this burden estimate or any other aspect of this collection of information, including suggestions for reducing this burden, to Washington headquarters Services, Directorate for Information Operations and Reports, 1215 Jefferson Davis Highway, Suite 1204, Arlington, VA 22202-4302, and to the Office of Management and Budget, Paperwork Reduction Project (0704-0188) Washington DC 20503.			
1. AGENCY USE ONLY *(Leave blank)*	**2. REPORT DATE** December 2002	**3. REPORT TYPE AND DATES COVERED** Master's Thesis	
4. TITLE AND SUBTITLE: Title (Mix case letters) The Influence of Shallow Water Variability on Short range Water Bourne Propagation			**5. FUNDING NUMBERS**
6. AUTHOR LT Stephen C. Karpi			
7. PERFORMING ORGANIZATION NAME(S) AND ADDRESS(ES) Naval Postgraduate School Monterey, CA 93943-5000			**8. PERFORMING ORGANIZATION REPORT NUMBER**
9. SPONSORING /MONITORING AGENCY NAME(S) AND ADDRESS(ES) N/A			**10. SPONSORING/MONITORING AGENCY REPORT NUMBER**
11. SUPPLEMENTARY NOTES The views expressed in this thesis are those of the author and do not reflect the official policy or position of the Department of Defense or the U.S. Government.			
12a. DISTRIBUTION / AVAILABILITY STATEMENT Approved for public release; distribution is unlimited.			**12b. DISTRIBUTION CODE**

13. ABSTRACT ***(maximum 200 words)***

Interest in enhancing the forecasting capabilities of both active and passive sonar systems employed in littoral regions has greatly escalated over the past 10 years. This requires a need for improvements in the general understanding of the influence of shallow water variability on acoustic propagation. This work examines the influence on the relatively short-range water-bourne propagation paths of shallow water variability. Both internal wave fluctuations and random sound speed perturbations will be considered The effects of littoral variability on acoustic propagation will be quantified in terms of spatial (vertical) coherence functions. Since the effects of the water-column variability is of interest, the direct water-bourne propagation path will be solely analyzed. The data to be examined will be generated numerically based on an acoustic propagation model employing environmental data taken from the East China Sea as part of the ONR-sponsored ASIAEX experiments.

14. SUBJECT TERMS Shallow water variability, range independent, range dependence, internal wave perturbations, vertical coherence			**15. NUMBER OF PAGES** 71
			16. PRICE CODE
17. SECURITY CLASSIFICATION OF REPORT Unclassified	**18. SECURITY CLASSIFICATION OF THIS PAGE** Unclassified	**19. SECURITY CLASSIFICATION OF ABSTRACT** Unclassified	**20. LIMITATION OF ABSTRACT** UL

NSN 7540-01-280-5500 Standard Form 298 (Rev. 2-89)
Prescribed by ANSI Std. 239-18

THIS PAGE INTENTIONALLY LEFT BLANK

Approved for public release; distribution is unlimited.

THE INFLUENCE OF SHALLOW WATER VARIABILITY ON SHORT RANGE WATER BOURNE PROPAGATION

Stephen C. Karpi
Lieutenant, United States Navy
B.S., University of Arizona, 1995

Submitted in partial fulfillment of the
requirements for the degree of

MASTER OF SCIENCE IN ENGINEERING ACOUSTICS

from the

NAVAL POSTGRADUATE SCHOOL
December 2002

Author: Stephen C. Karpi

Approved by: Kevin B. Smith, Thesis Advisor

Peter H. Dahl, Co-Advisor

Kevin B. Smith, Chairman
Engineering Acoustics Academic Committee

THIS PAGE INTENTIONALLY LEFT BLANK

ABSTRACT

Interest in enhancing the forecasting capabilities of both active and passive sonar systems employed in littoral regions has greatly escalated over the past 10 years. This requires a need for improvements in the general understanding of the influence of shallow water variability on acoustic propagation. This work examines the influence on the relatively short-range water-bourne propagation paths of shallow water variability. Both internal wave fluctuations and random sound speed perturbations will be considered The effects of littoral variability on acoustic propagation will be quantified in terms of spatial (vertical) coherence functions. Since the effects of the water-column variability is of interest, the direct water-bourne propagation path will be solely analyzed. The data to be examined will be generated numerically based on an acoustic propagation model employing environmental data taken from the East China Sea as part of the ONR-sponsored ASIAEX experiments.

THIS PAGE INTENTIONALLY LEFT BLANK

TABLE OF CONTENTS

LIST OF FIGURES

LIST OF TABLES

THIS PAGE INTENTIONALLY LEFT BLANK

ACKNOWLEDGMENTS

The two years of education received at the Naval Postgraduate School have been enriching on both a personal and career level. As with any project that accumulates this amount of time, there are many people to thank.

First, I would like to thank Angela, my wife, for her constant support and encouragement throughout my military career. Her divine character and patience gives me the motivation and power to accomplish anything. I would also like to thank my four children, Calton, Nathaniel, Anna and Lucas, who have enlightened my life every day from their little smiles. A special thanks is merited to all the friends and family who have supported my wife and me over the years.

My utmost appreciation goes to Professor Kevin Smith, my thesis advisor for his guidance and patience, which made this thesis a success. His knowledge of signal processing as well as acoustics was priceless throughout this work.

My appreciation also goes to Dr. Peter Dahl, APL at the University of Washington, the thesis second reader for his timely support and advice.

There are too many others to list who have contributed to this work but some of them include: CDR John Joseph (USW Curricular Officer), Professor James Sanders (Academic Associate), and last but certainly not least Eva Anderson (Code 35 Educational Specialist).

THIS PAGE INTENTIONALLY LEFT BLANK

I. INTRODUCTION

With the traditional 'blue water' Navy now carrying out its transition into the coastal 'littoral' regions, shallow-water acoustic propagation is becoming the topic of interest. Deep isothermal layers and the deep sound-channel axis are concepts operationally used less frequently, being replaced by internal waves, random perturbations and shallow-water reverberation. The complex littoral operating environment is manipulated by both temporal and spatial fluctuations, which can alter the existing sound speed profile. These sound speed fluctuations can greatly influence sonar system performance and ability to accurately detect an acoustic signal.

The understanding and influence of these sound speed perturbations on littoral acoustic propagation is important. In coastal regions various factors affect the propagation of short-range acoustical signals such as the wind, tidal effects, offshore currents and even river out-flows. Characteristic lengths range from meters (e.g. non-linear internal waves) to several kilometers (e.g. internal tides and mesoscale structures) with typical periods going from minutes to days. Furthermore, surface and internal mixed layers can be established, and significantly change, over the range of minutes developing a homogeneous well-mixed water column and erasing all the other structures.[(1)] The temporal and spatial independent environments assumed by the Navy in most littoral regions can result in faulty sonar system predictions and performance.

The Office of Naval Research (ONR) has recently provided funding for extended research in shallow water acoustic propagation and forecasting. This funding was used in the ASIAEX East China Sea experiment conducted from 29 May 2001 to 9 June 2001. A science team from the Applied Physics Laboratory (APL) at the University of Washington (UW) and several other teams deployed a variety of instruments used to measure short-range acoustic propagation, scattering and the measurement of the variable environmental parameters in the East China Sea. "The main goal of the ASIAEX was to contribute to a more fundamental understanding of ocean acoustic propagation and scattering in shallow-water regions while fostering cooperative research among Pacific Rim nations."[(2)] The East China Sea possesses a complex littoral environment, similar to other littoral regions where acoustic propagation is of interest. The ASIAEX produced an

invaluable set of measurements on environmental variability and littoral acoustic propagation recordings, which will be analyzed by several institutions in the near future.

The Naval Postgraduate School will contribute to the shallow-water acoustic research with the work presented in this thesis. To maintain consistency with the ASIAEX parameters, the same environmental and array geometry will be used in all the models allowing for easy comparison in the future. A vertical line array (VLA) comprising of two 4-element clusters will be simulated in a 110-meter shallow water region. The upper and lower receiver clusters are located at 26 and 52 meters in depth, separated from the source by a range of 460 meters. A 4 kHz, 8 kHz, 16 kHz and 20 kHz 2 msec pulse will be transmitted from the source. The analysis will consist of both continuous wave (CW) and broadband (BB) signals.

The objective of this thesis is to examine the influence of sound speed perturbations, consistent with that of the shallow-water variability present in littoral regions. The focus will be primarily on the relatively short-range acoustic propagation and scattering of the direct water-bourne propagation path. Since the actual variability of the environment is unpredictable and random, several different range-dependent environments will be employed and their results analyzed. The influence of internal wave fluctuations will be considered by attempting to model the propagation effects of a single-sinusoid and complex multiple-sinusoid range-dependent environment. In addition to internal wave fluctuations, a random sound speed perturbation environment will be incorporated into this analysis. To determine the amount of signal degradation occurring due to the variability of the environment, the vertical coherence will be examined. This will provide information about the signal decorrelation that occurs during the short propagation of the direct path signal. The correlation results of each environment will be compared to the correlation of a simple range-independent sound speed profile environment.

In the past few years, several students at the Naval Postgraduate School have examined shallow water acoustics using the Monterey-Miami Parabolic Equation (MMPE) propagation model.[3] The MMPE model was developed by Smith and Tappart in 1996 and has since then been improved to include perturbations in the sediment floor along with interface interaction. Since the interest of this thesis is primarily in the water

column, the MMPE model has been adapted to incorporate various sound speed fluctuations into the water column. The baseline sound speed profile used in each program was based on actual data taken during the East China Sea portion of the ASIAEX. All of the signal and analytical post possessing was done using MATLAB code developed for this thesis. Data evaluations were conducted by comparing the four simulated environments. Future work will incorporate more realistic models of ocean volume turbulence and effects on sound speed. In addition to this, statistical results from the MMPE model will eventually be compared with the actual data from the APL at UW.

THIS PAGE INTENTIONALLY LEFT BLANK

II. NUMERICAL METHODS AND IMPLEMENTATION

A. MIAMI-MONTEREY PARABOLIC EQUATION (MMPE) MODEL

The parabolic equation (PE) method was introduced into underwater acoustics in the early 1970's by Tappert.[4] This numerical approach to solving the wave equation has become a popular method in underwater acoustics. The MMPE Model used in this experiment is based upon this parabolic approximation of the wave equation. The application of the PE method applied to underwater wave-propagation is the subject of this chapter.

We begin by defining the time harmonic acoustic pressure field represented in the cylindrical coordinate system assuming azimuthal symmetry,

$$P\left(r,z,\omega t\right)=p\left(r,z\right)e^{-i\omega t}. \tag{1}$$

Since the ocean can be portrayed as a thin waveguide on the surface of the planet exhibiting weak azimuthal symmetry, a cylindrical coordinate system is the logical choice and azimuthal symmetry will be assumed.

Substituting Eq. (1) into the wave equation in cylindrical coordinates leads to the Helmholtz equation,

$$\nabla^2 p(r,z)+\frac{\omega^2}{c(r,z)^2}p(r,z)=0, \tag{2}$$

where

$$\nabla^2=\frac{1}{r}\frac{\partial}{\partial r}r\frac{\partial}{\partial r}+\frac{\partial^2}{\partial z^2}. \tag{3}$$

Cylindrical spreading is assumed to dominate the propagation and so the pressure field can be defined by [3]

$$p(r,z)=\frac{1}{\sqrt{r}}u(r,z). \tag{4}$$

This $1/\sqrt{r}$ term will account for cylindrical spreading and u(r,z) will represent the two-dimensional pressure field. Substituting Eq. (4) into Eq. (2) yields the uncoupled azimuth approximation(UNCA), [3]

$$\frac{\partial^2 u}{\partial r^2}+\frac{\partial^2 u}{\partial z^2}+k_o{}^2\left(n^2+\frac{1}{4k_o{}^2 r^2}\right)u=0\,. \tag{5}$$

The Helmholtz equation can be further simplified by introducing the operator notation

$$Q_{op}=(\mu+\varepsilon+1)^{\frac{1}{2}}, \tag{6}$$

and

$$P_{op}=\frac{\partial}{\partial r}\,, \tag{7}$$

where

$$\varepsilon=n^2-1\,,\qquad n=\frac{c_0}{c}\,,\quad \mu=\frac{1}{k_o^2}\frac{\partial^2}{\partial z^2}\,, \tag{8}$$

and c_0 is the reference sound speed typical of the ocean volume. This allows the uncoupled azimuth approximation to be simplified in the form

$$(P_{op}{}^2+k_o{}^2 Q_{op}{}^2)u=0\,. \tag{9}$$

It has been shown [3] that the outward propagating field, Ψ, is defined by

$$u=\frac{1}{\sqrt{Q_{op}}}\Psi\,, \tag{10}$$

and satisfies the one-way parabolic equation of the form

$$-ik_o{}^{-1}\frac{\partial\Psi}{\partial r}=Q_{op}\Psi\,. \tag{11}$$

Assuming the backscattered energy is negligible, Eq. (11) represents the complete description of the forward propagating acoustic energy in the waveguide.[3]

The acoustic pressure may now be defined as,

$$p(r,z) = P_o \sqrt{\frac{R_o}{r}} Q_{op}^{-1/2} \psi(r,z) e^{ik_o r}, \tag{12}$$

where $\psi(r,z)$ is the envelope function or PE field function. The parabolic equation for the field function is then defined by

$$\frac{\partial \psi}{\partial r} = -ik_o \psi + ik_o Q_{op} \psi = -ik_o H_{op} \psi, \tag{13}$$

where

$$H_{op} = 1 - Q_{op} \tag{14}$$

is a Hamiltonian-like operator, which defines the evolution of the PE field function in range.

The relationship between values of ψ at different ranges can be defined by a marching algorithm of the form

$$\psi(r + \Delta r) = \Phi(r) \psi(r), \tag{15}$$

where $\Phi(r)$ is a unitary operator that progresses the solution out in range. The MMPE model employs a split-step Fourier (PE/SSF) method to provide a representation of this propagator $\Phi(r)$. The (PE/SSF) implementation of the parabolic equation works well in the model primarily due to its speed and simplicity, particularly in range-dependent media, which is the basis of this work. The propagator $\Phi(r)$ can then be shown to take the form [3]

$$\Phi(r) = \left[e^{-ik_o \frac{\Delta r}{2} U_{op}(r + \Delta r)} \right] \left[e^{-ik_o \Delta r T_{op}} \right] \left[e^{-ik_o \frac{\Delta r}{2} U_{op} r} \right], \tag{16}$$

where

$$U_{op} = -[n - 1], \tag{17}$$

and

$$\hat{T}_{op} = 1 - \left[1 - \left(\frac{k_z}{k_o} \right)^2 \right]^{1/2}. \tag{18}$$

This method is used in the MMPE model since this scheme has been shown to provide third-order accuracy in Δr.[3] The discrete Fast Fourier Transform (FFT) is being used in the code assuming the convention

$$\Psi(z) = FFT(\dot{\Psi}(k_z)) \tag{19}$$

and

$$\dot{\Psi}(k_z) = IFFT(\Psi(z)). \tag{20}$$

The PE/SSF implementation can then be represented by

$$\psi(r+\Delta r, z) = e^{-ik_o \frac{\Delta r}{2} U_{op}(r+\Delta r, z)} FFT\left[e^{-ik_o \Delta r \hat{T}_{op}(k_z)} * IFFT\left(e^{-ik_o \frac{\Delta r}{2} U_{op}(r,z)} \psi(r,z) \right) \right]. \tag{21}$$

B. IMPLEMENTATION OF RANGE DEPENDENT ENVIRONMENTS IN MMPE

Having described the concepts of the MMPE model, we will now focus on the theoretical methods of generating various perturbations in the water column. The incorporation of these effects into the MMPE model is also discussed. The simple sinusoidal internal wave fluctuations are based on perturbations defined by the Shallow Water Acoustic Modelling Workshop (SWAM99).[5] The formulation of the small-scale, turbulent-like perturbation theory is based on a simple 2-D spectral model.

1. Single Sinusoidal Internal Wave Fluctuations

A simple sinusoidal internal wave fluctuation was entered into the volume of the water column to create some short-range variability. The equation used has the form

$$\delta c(r,z) \approx C\left(\frac{z}{B}\right)\left(1 - e^{\left(\frac{z-z'}{B}\right)}\right)\cos(Kr), \tag{22}$$

where B=60m, z'=70m and K=2π/100m. C is defined as a constant to achieve the desired maximum amplitude of our perturbation. The exponential term was inserted to ensure that the perturbations were present from the surface to 70 meters, with the perturbations decaying to zero at the surface and below 70 meters. (For depths below 70 meters, no perturbations were introduced.)

2. Multiple Sinusoidal Internal Wave Fluctuations

In an attempt to further complicate the rather simple symmetrical internal wave, several sinusoids were introduced into the environment using the expression

$$\delta c(r,z) \approx \sum_{n=1}^{5} \frac{C}{n}\left(\frac{z}{B}\right)\left(1-e^{\left(\frac{z-z'}{B}\right)}\right)\cos(Krn) \quad , \tag{23}$$

where again B=60m, z'=70m and K=2π/100m. You can see here that as the index increases the scale and amplitude of the sound speed perturbation decreases. This is generally consistent with internal wave observations.

3. Turbulent Sound Speed Fluctuations

To create non-symmetrical random perturbations in our environment, the introduction of turbulent-like perturbations based on a random realization of a 2-D variability spectrum is introduced. The form of the 2-D spectrum used is adapted from previous work [6] that employed the spectrum to create 2-D sediment variability. While this form is not entirely appropriate as a model of water column turbulence variability, it is rather generic and allows for a first-glimpse analysis of the potential effects of such fluctuations. Future work will incorporate more realistic turbulence spectrum for the water column.

The 2-D vertical plane (r,z) spectrum to be employed here has the generic form

$$W_{\delta c,2D}(K,M) = \alpha\left(\Lambda^2 K^2 + M^2\right)^{-3/2}, \tag{24}$$

where K is the horizontal component of the wavenumber, M is the vertical component of the wavenumber, and Λ represents a scaling of the anisotropy of the fluctuations due to

stratification or layering. For this analysis, a value of $\Lambda = 5$ was chosen. The scaling parameter α is inconsequential since the resulting perturbation will simply be rescaled to produce a pre-determined value for the rms perturbation. To generate 2-D vertical volume sound speed fluctuation realizations, we define a realization as

$$c_0 \delta c(x,z) = \iint S_{\delta c}(K,M) e^{iKr} e^{iMz} dK dM \,, \tag{25}$$

where

$$S_{\delta c}(K,M) = \left[W_{\delta c,2D}(K,M) \right]^{1/2} * \left[A(K,M) e^{i\theta(K,M)} \right] \,. \tag{26}$$

The second term in Eq. 26 introduces a random amplitude and phase into the spectrum defined by

$$\theta(K,M) = 2\pi r_1(K,M) \tag{27}$$

and

$$A(K,M) = \sqrt{-\ln(r_2(K,M))} \tag{28}$$

where both $r_1(K,M)$ and $r_2(K,M)$ are now a *matrix* of uniformly distributed random numbers in [0,1]. In practice, we use

$$W_{\delta c,2D}(K,M) \propto \left(\Lambda^2 K^2 + M^2 \right)^{-\frac{\beta_\delta}{2} - 1} \,, \tag{29}$$

and rescale by the appropriate rms values. We then take the FFT of the spectrum and use the real portion for the MMPE model. These are the generic spectral models used in generating the realizations for implementation in the MMPE model.

C. TIME-DOMAIN PROCESSING

1. Time-Domain Analysis

We will begin our analysis by presenting the pressure field in the simplified form

$$p(r,z,f) = \frac{1}{\sqrt{r}} \psi(r,z,f) e^{ik_o r} \,, \tag{30}$$

where $\psi(r,z,f)$ is the normalized PE field function defined to yield zero transmission loss at one meter from the source. The pressure field in the time domain is then defined by

$$p(r,z,t) = \int_{-\infty}^{\infty} A(f)\, p(r,z,f) e^{-i2\pi ft} df\,, \tag{31}$$

where A(f) is the source amplitude function. Substituting $p(r,z,f)$ into Eq. (31) produces

$$p(r,z,t) = \frac{1}{\sqrt{r}} \int_{-\infty}^{\infty} A(f)\psi(r,z,f) e^{ik_o r} e^{-i2\pi ft} df\,. \tag{32}$$

Since $k_o = \omega / c_o$, this may be written

$$p(r,z,t) = \frac{1}{\sqrt{r}} \int_{-\infty}^{\infty} A(f)\psi(r,z,f) e^{i2\pi f\left(\frac{r}{c_o}\right)} e^{-i2\pi ft} df = \frac{1}{\sqrt{r}} \int_{-\infty}^{\infty} A(f)\psi(r,z,f) e^{-i2\pi f\left(t-\frac{r}{c_o}\right)} df \tag{33}$$

By defining the reduced time, $T = \left(t - \frac{r}{c_o}\right)$, the above equation gives

$$p(r,z,T) = \frac{1}{\sqrt{r}} \int_{-\infty}^{\infty} A(f)\psi(r,z,f) e^{-i2\pi fT} df\,. \tag{34}$$

Furthermore, noting that the amplitude function A(f) is only non-zero when

$$\left(f_c - \frac{BW}{2}\right) < f < \left(f_c + \frac{BW}{2}\right), \tag{35}$$

we can simplify the integral to

$$p(r,z,T) = \frac{1}{\sqrt{r}} \int_{f_c - \frac{BW}{2}}^{f_c + \frac{BW}{2}} A(f)\psi(r,z,f) e^{-i2\pi fT} df\,. \tag{36}$$

In order to accommodate this using FFTs, the pressure field must be base-banded around fc. This is accomplished by introducing the variable $f' = f - f_c$, thus yielding

$$p(r,z,T) = \frac{1}{\sqrt{r}} \int_{-\frac{BW}{2}}^{\frac{BW}{2}} A(f'+f_c)\psi(r,z,f'+f_c)e^{-i2\pi(f'+f_c)T}df'. \quad (37)$$

Since f_c is a constant, Eq(38) can be further simplified to,

$$p(r,z,T) = \frac{e^{-i2\pi f_c T}}{\sqrt{r}} \int_{-\frac{BW}{2}}^{\frac{BW}{2}} A(f'+f_c)\psi(r,z,f'+f_c)e^{-i2\pi f'T}df'. \quad (38)$$

Defining $p'(r,z,T)$ as the base-banded pressure signal

$$p'(r,z,T) = \frac{1}{\sqrt{r}} \int_{-\frac{BW}{2}}^{\frac{BW}{2}} A(f'+f_c)\psi(r,z,f'+f_c)e^{-i2\pi f'T}df', \quad (39)$$

our time-domain base-banded pressure signal can be simplified to

$$p(r,z,T) = e^{-i2\pi f_c T} p'(r,z,T), \quad (40)$$

noting that $e^{-i2\pi f_c T}$ acts as a phase multiplier for the signal.

The discretely sampled transform pairs are now

$$p'(r,z,T_m) \Leftrightarrow \frac{1}{\sqrt{r}} A(f_n)\psi(r,z,f_n). \quad (41)$$

Based on standard variable relationships of FFT's, the corresponding variables here are

$$f_n = \frac{-N}{2}\Delta f + (n-1)\Delta f \quad (42)$$

$$T_m = \frac{-N}{2}\Delta t + (m-1)\Delta t \quad (43)$$

for m, n = 1… N.

To perform broadband as well as CW analysis, several center frequencies were chosen for good representation and to keep consistent with the values used during the ASIAEX processing. The center frequencies examined were 4kHz, 8kHz, 16kHz, and 20kHz all using a bandwidth of 8184 Hz. This bandwidth was divided into 1024 discrete propagation frequencies. The frequency step is then

$$\Delta f = \frac{BW}{N-1} = \frac{8184}{1024-1} \sim 8Hz, \tag{44}$$

and the time increment is

$$\Delta t = \frac{T}{(N-1)} = \frac{1}{(N-1)\Delta f} = \frac{1}{BW} = \frac{1}{8184} \sim 0.122ms. \tag{45}$$

The number of indices required to produce a 2 ms pulse can easily be found by $n_{pulse} = 2m\sec/\Delta t$.

2. Creation of the Source Amplitude Spectrum A(f)

In order to create a proper source amplitude function, it is necessary to consider a combination of the 2 msec pulse spectrum of the transmitted signal and the receiver system response filter, which defines the center frequency. To produce a 2 msec square pulse in the time domain, we can calculate the number of indices necessary using our time increment, $n_{pulse} = 16$. The simple square pulse signal takes the form,

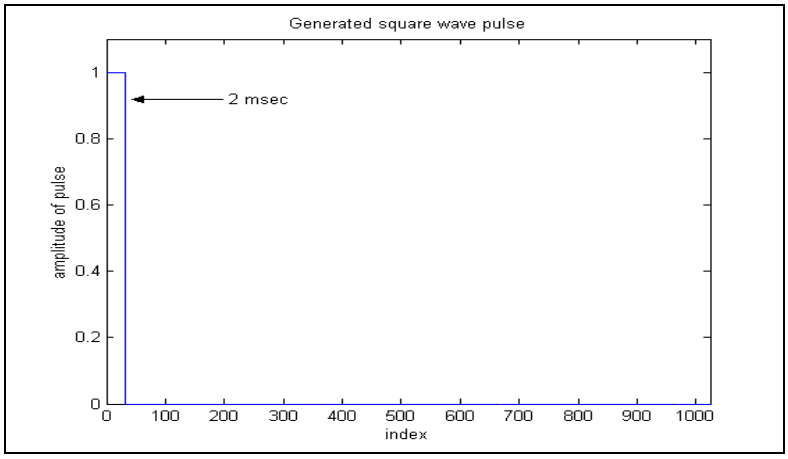

Figure 1. Initial 2 msec Square Pulse

This pulse is now padded to create a spectrum with the required length of 1024.

The transformation of the square pulse to the frequency domain via an FFT can be seen in Fig. 2.

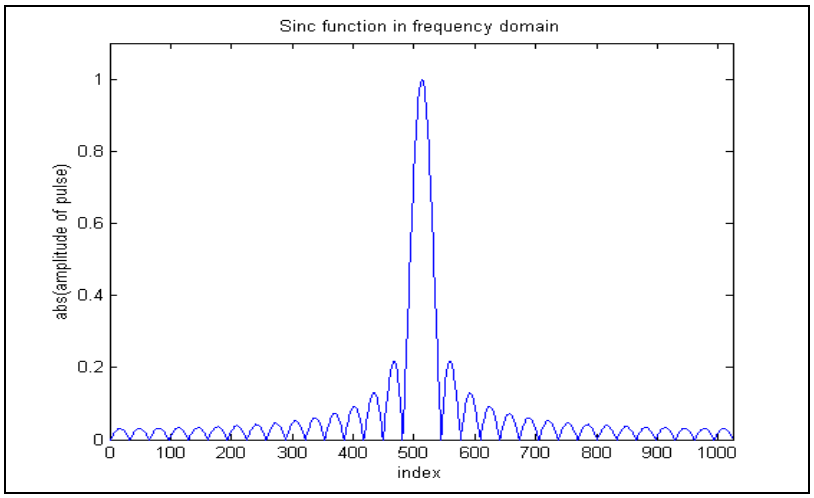

Figure 2. Resulting Pulse in Frequency Domain, i.e. Sinc Function

The pulse spectrum takes the expected form of the sinc function, which is defined as $\mathrm{sinc}(x) = \frac{\sin(\pi x)}{\pi x}$.

During analysis of the ASIAEX data, the APL team from the University of Washington attempted to remove some of the out of band noise by applying a digital band-pass filter to the signal. During the filtering process they preserved approximately 10kHz of bandwidth, using roughly a +/- 5 kHz band over the center frequency. This was not achievable for the 4 kHz and 20 kHz center frequencies due to negative frequency limitations and the Nyquist frequency, respectfully. Therefore, the band-pass filter was not always applied with the center frequency located in the middle of the window. The difference between the center of the filter and the actual center frequency was accounted for in this analysis, in order for the model results to be as consistent as possible with the observations. The following table lists the band-pass digital filter bandwidths that were used in the processing of the measured data.

ASIAEX Carrier Freq. (kHz)	ASIAEX Filter Freq. Min (kHz)	ASIAEX Filter Freq. Max (kHz)	ASIAEX Center of Filter (kHz)	MMPE Shift required (kHz)
4	2	12	7	3
8	5	14	9.5	1.5
16	12	20	16	0
20	15	23	19	1

Table 1. Approximate Filter Bandwidths Applied to the Spectrum in the Data Processing and the Required Shift

The next step was to construct the system response band-pass filter and apply it to the model pulse spectrum. The application and choice of the appropriate signal-processing window needed to addressed. Combining a simple rectangular window and a Hanning window taper at the ends created the models' system response filter. The rectangular window is located in the center of the spectrum allowing the majority of the signal to pass. The Hanning window that was used can be defined as

$$w[k] = \frac{1}{2}\left(1 - \cos\left(2\pi \frac{k}{n+1}\right)\right), \qquad \text{k=1,…,n} \tag{46}$$

and its shape can be seen in Fig. 3.

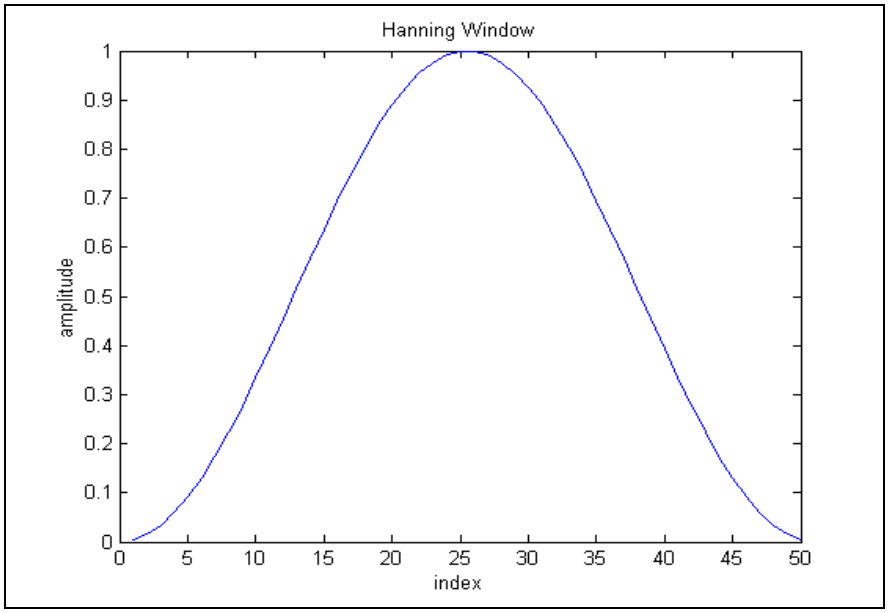

Figure 3. Typical Hanning Signal-Processing Window

The Hanning window was divided in half and applied to the ends of the rectangular window to minimize the side-lobe suppression. The system response filter was then used as a multiplier on our 2 msec pulse spectrum completing the source amplitude function A(f). A generic example of the amplitude function showing a shifted pulse spectrum within the response filter can be seen in Fig. 4.

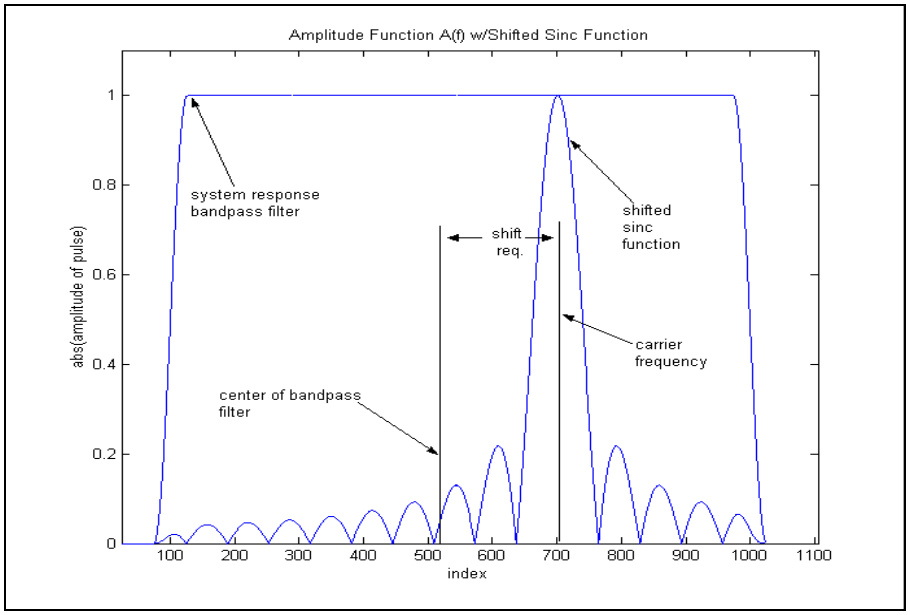

Figure 4. Amplitude Function Comprised with Shifted Sinc and System Response Filter

III. MODELING GEOMETRY AND ENVIRONMENT

A. MODEL AND ARRAY GEOMETRY

For purposes of modeling, the source and receivers were placed in a 110-meter water column with a range separation of 460 meters. A vertical line array (VLA) was chosen for the receiving array containing two, 4-element clusters. Element separation within each of the clusters is 13 cm, 30 cm and 60 cm making each element approximately one meter. The top element of the upper cluster was positioned at 26 meters and the top element of the lower cluster was positioned at 52 meters. The source was modeled from two different depths, 26 meters and 50 meters. To perform the broadband analysis, center frequencies of 4kHz, 8kHz, 16kHz and 20kHz were used with a bandwidth of 8184Hz. Figure 5 shows the VLA, its component separation and geometry

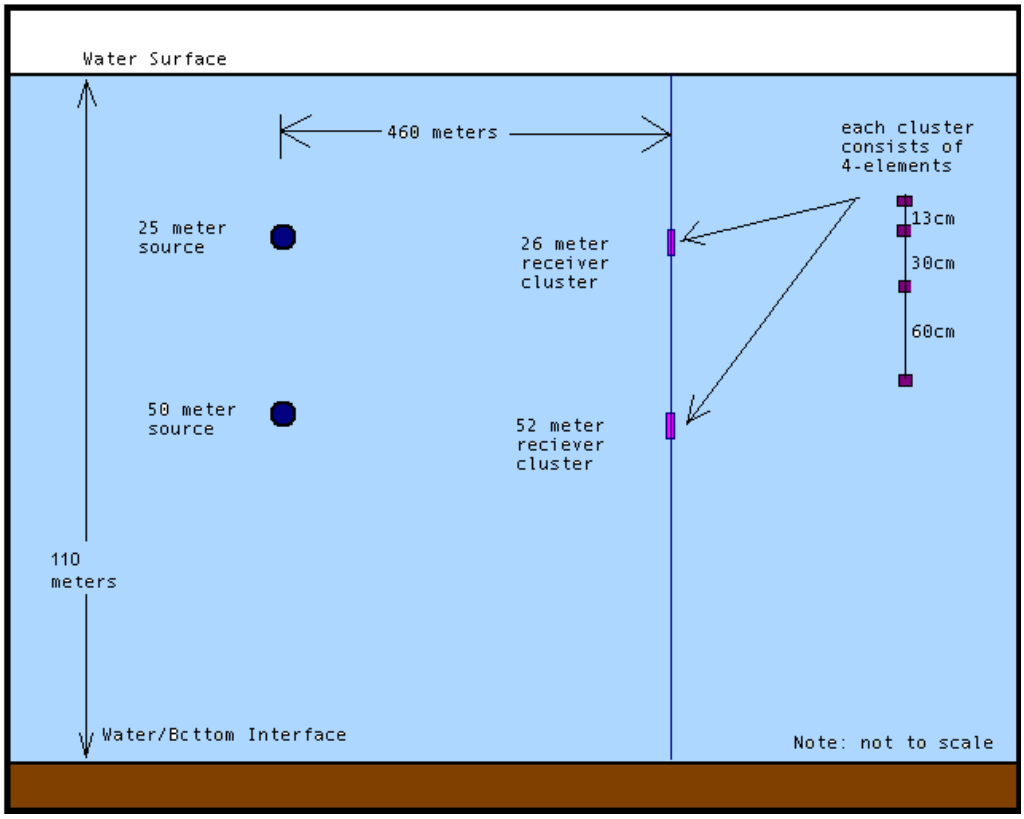

Figure 5. Geometry and Spacing of Arrays

B. ENVIRONMENTAL MODELS

Attempting to create an environment that accurately portrays the dynamic perturbations of a littoral region was cumbersome. The variations in a littoral sound speed profile have both temporal and spatial dependence. Effects of the wind, tides, and currents result in the rapid mixing of thermal layers and unpredictability. Since we are primarily interested in the direct water-bourne path the modeling of the variability in the water column is essential to our work.

1. Sound Speed Profile

Seven representative sound speed profiles were obtained from the ASIAEX database and are shown in Figure 6. Of the seven profiles shown, ssp029 was chosen primarily because the location was closest to the center of the ASIAEX operating area. This profile was used throughout the modeling runs as the baseline sound speed profile and Range Independent environment see Figure 7, from which all other modeling environments evolved.

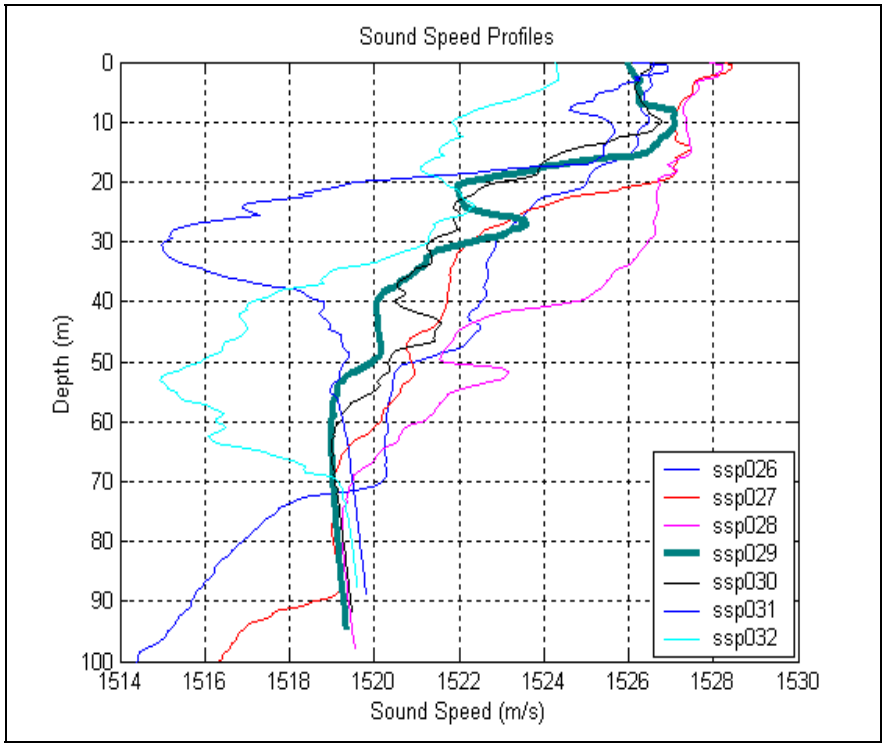

Figure 6. Typical Sound Speed Profiles of East China Sea

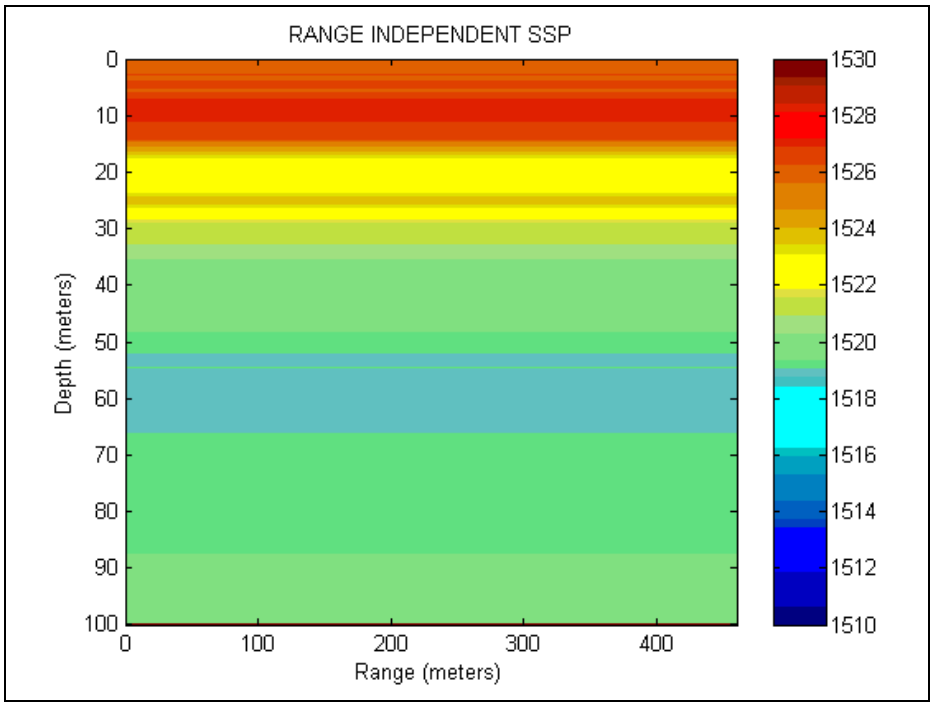

Figure 7. Range Independent Environment from ssp029

1. Range-Dependent Perturbation Environments

The first method of simulated variability was the integration of simple sinusoidal internal waves into the water column. As previously discussed, two variations of internal wave environments were created for this work a single sinusoid perturbation and multiple sinusoids perturbation. The third method of simulated variability was the introduction of turbulent sound speed fluctuations into the water column producing random perturbations. The effects of the volumetric sound speed variability on the range-independent environment are illustrated in the figures on the next page. For each type of perturbation environment, several magnitudes of sound speed fluctuation were used in the model during the experiment. This analysis covered a wide range of frequencies (4kHz –20kHz) and the different magnitudes were necessary to produce a measurable decorrelation. The magnitudes used during the model runs are shown in Table 1.

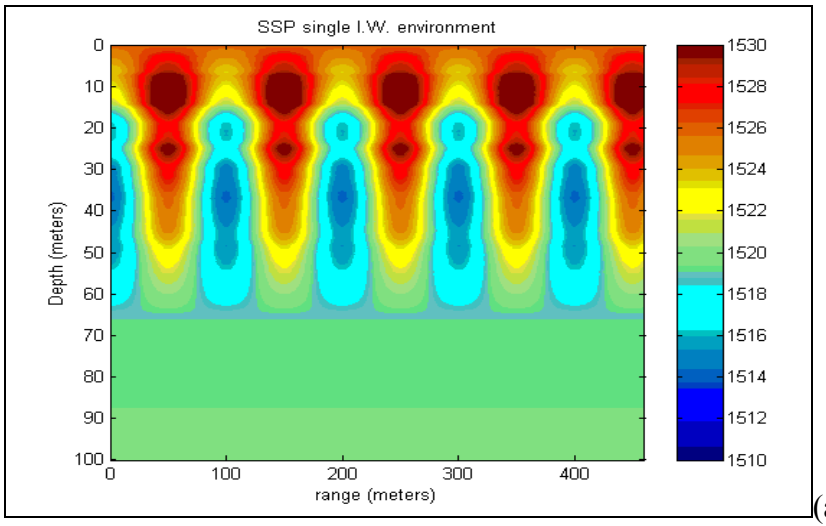

(a)

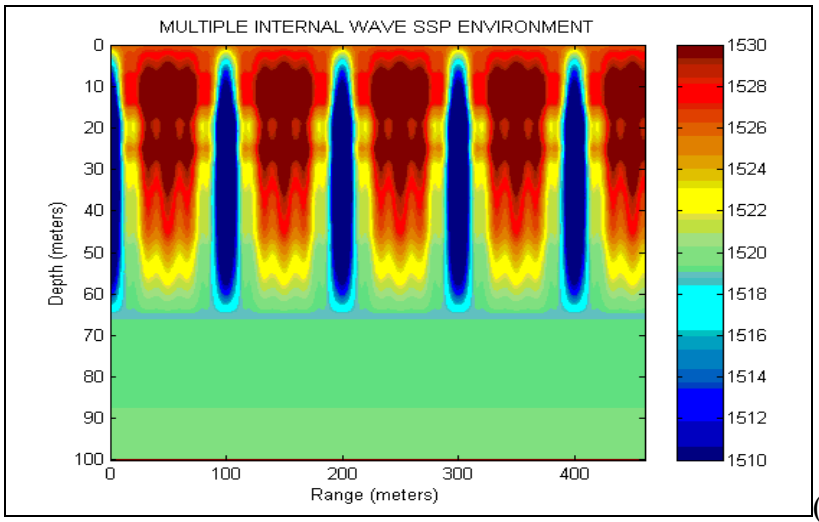

(b)

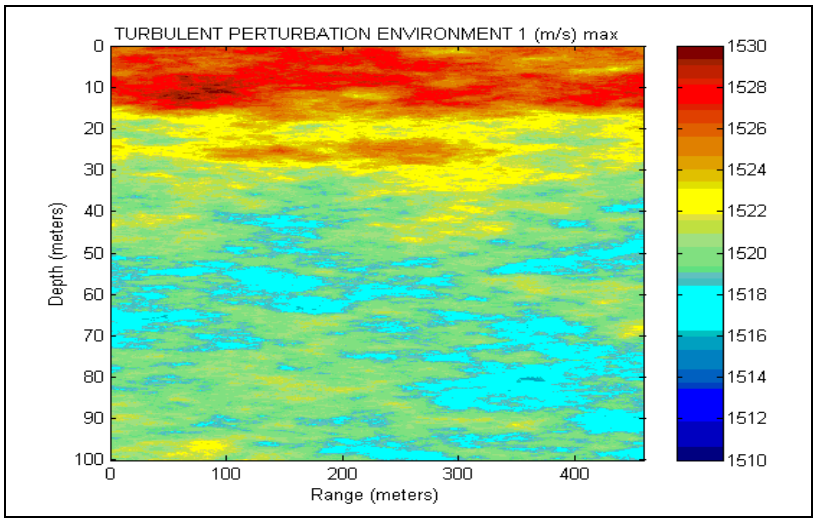

(c)

Figure 8. (a)Single Sinusoid, (b)Multiple Sinusoid and (c)Turbulent Perturbation Environments

2. Different Sound Speed Magnitudes in Environment.

	4 kHz	**8kHz**	**16kHz**	**20kHz**
Range-Independent (ssp029) RI	RI	RI	RI	RI
Range-Dependent 1- Sinusoid peak magnitude	10(m/s)	10(m/s)	10(m/s)	10(m/s)
Range-Dependent 5-Sinusoids peak magnitude	2.0(m/s) 10.0(m/s)	Not Done	2.0(m/s) 10.0(m/s)	Not Done
Range-Dependent Turbulent Perturbations rms magnitude	1.0(m/s) 2.5(m/s) 5.0(m/s)	1.0(m/s) 2.5(m/s) 5.0(m/s)	0.5(m/s) 0.75(m/s) 1.0(m/s)	0.25(m/s) 0.5(m/s) 1.0(m/s)

Table 2. Different Environments used for each Frequency

THIS PAGE INTENTIONALLY LEFT BLANK

IV. POST PROCESSING AND ANALYSIS

A. POST PROCESSING 1 - TRANSMISSION LOSS (TL)

The standard measure in underwater acoustics of the change in signal strength with range is transmission loss (TL).[7] Transmission loss can be considered the signal which is loss due to the sum of geometric spreading, refraction, interference and the loss due to attenuation in the ocean. The spreading loss is simply a geometrical effect describing how a signal is weakened as it propagates or expands from the source. Typical spreading laws used in underwater acoustics are spherical, $I \propto \frac{1}{4\pi R^2}$, and cylindrical, $I \propto \frac{1}{2\pi RD}$. The ocean's variable internal structure, combined with its surface and bottom boundaries, creates a complex propagating environment for acoustics. As sound propagates through a variable water column the underwater signal attenuates and will become absorbed, delayed, distorted and weakened. The absorption of sound is very multifaceted due to its dependence on salinity, temperature, range and frequency. Transmission loss is an important sonar quantity and will be used in this section to illustrate the strong effects of shallow water variability on the direct water-bourne propagation path.

The computation of TL will be used to show the signal loss and the arrival structure from the 50 m source at both the upper and lower receiver array clusters. In terms of the field function Ψ, the single frequency TL will be calculated according to

$$TL = -20\log\left[\frac{|p|}{p_o}\right] = -20\log\left[|\psi|\right] + 10\log\left[\frac{r}{R_o}\right], \tag{47}$$

where R_o is the reference range at 1 meter.

Implementing the MMPE model, the 4kHz, 8kHz, 16kHz and 20kHz frequencies were transmitted through each of the simulated shallow water environments. However, only the 4 kHz and 16 kHz model runs will be presented to prevent redundancy. The arrival structure was computed using both a broadband (BB) and continuous wave (CW)

frequency band. The broadband source transmits a frequency spectrum consistent with a 2 msec CW pulse and the solution was then stored at a range of 460 meters.

1. Range-Independent (RI)

The 4 kHz 2 msec pulse was transmitted through the RI environment and the TL plots were generated for the CW and BB case. The CW TL field is plotted along a single radial out to the range of 460 meters. The CW TL plot exhibits the presence of modal interference in the water column. Note that the short range, high angle shadows are sue simply to the wide-angle limitations of the PE starting field, but do no affect the propagation at the maximum range or the direct path contribution.

In the BB pulse arrival structure, it is clear that the direct path is separable from the reflected paths at both the 26m and 52 m depths of the receiving arrays. (although just barely at 26m) It is also perhaps interesting to note that the model predicts the existence of a head wave arrival at the deepest depths in the water column. Unfortunately, no data was recorded at such depths to confirm this phenomenon. Higher angle paths are observed to reflect from the ocean surface and bottom and arrive at later times. In some cases, the numerical limitations of the time window create a wrap-around effect on the latest arrivals, but this also will have no impact on the processing of the direct path data.

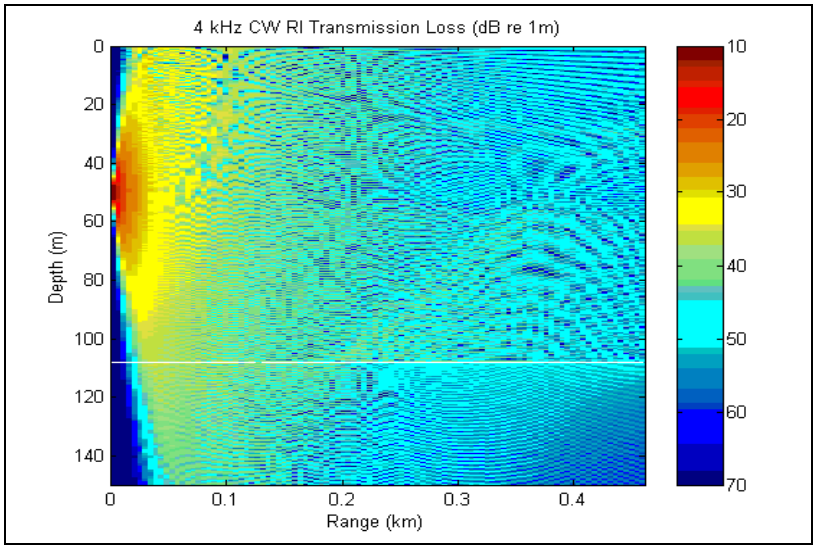

(a)

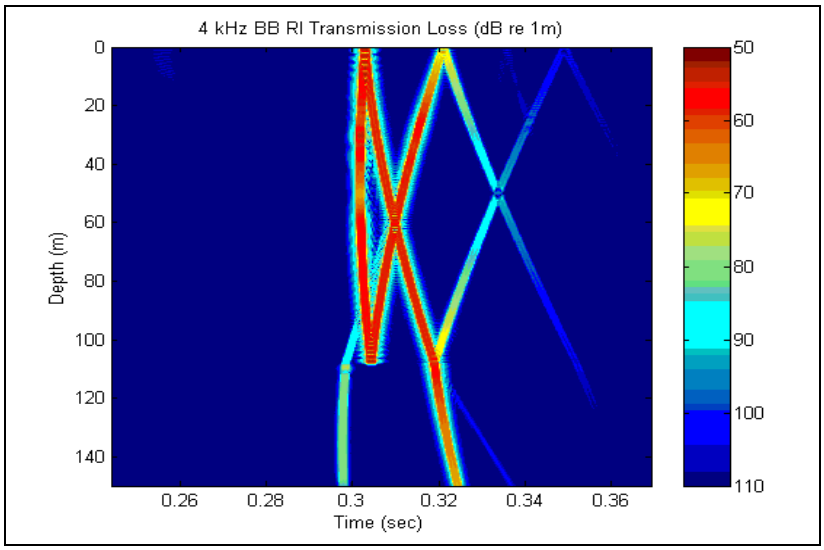

(b)

Figure 9. Range-Independent Transmission Loss (a) 4 kHz CW signal (b) 4 kHz 2mes BB pulse

To examine the propagation structure at higher frequencies in this range-independent environment, the results of the 16 kHz source calculation are shown below.. Both the CW and BB plots possess similar arrival structure and propagation losses as the 4 kHz source. The transmission of the higher frequency signals in all the environments produced more multi-path arrival structure and a weaker head wave due to more attenuation in the floor sediment. It may be anticipated that the shorter wavelength of the 6 kHz pulse will undergo more refractive losses as the sound speed fluctuations are added into the environment.

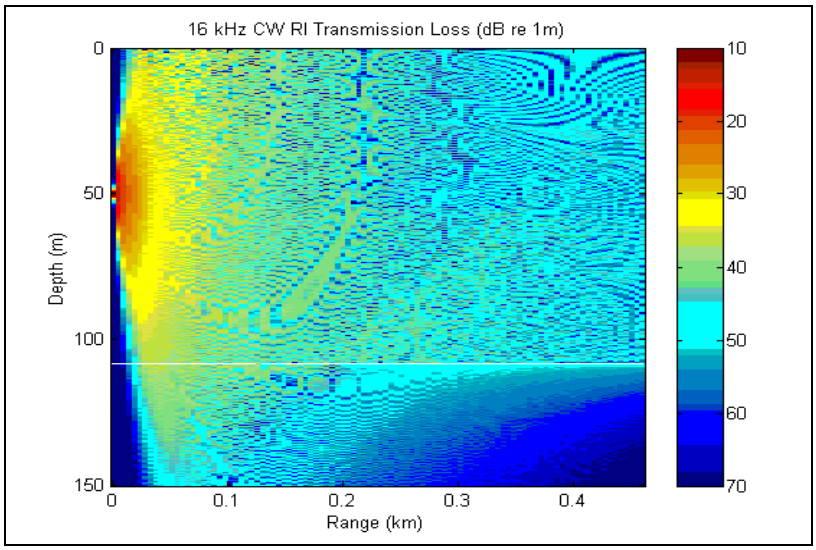

(a)

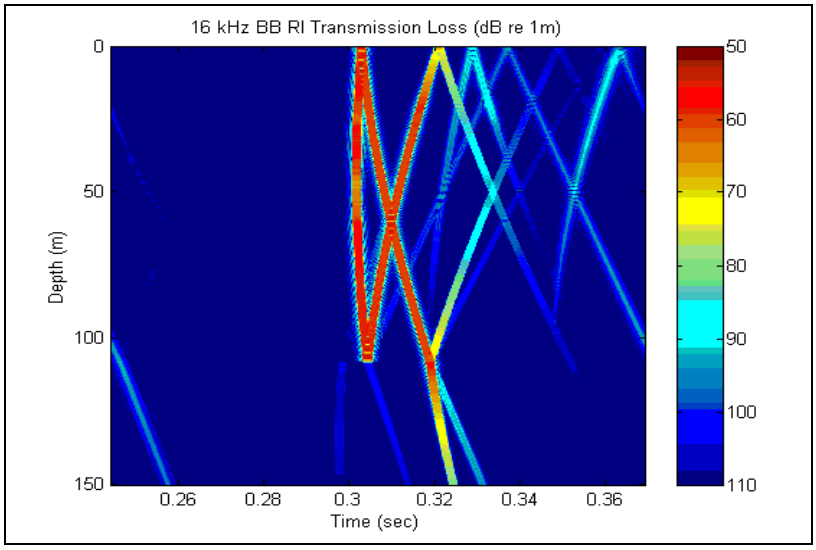

(b)

Figure 10. Range-Independent Transmission Loss (a) 16 kHz CW signal (b) 16 kHz 2 msec BB pulse

2. Range-Dependent (RD) Single Sinusoid

The range-dependent single sinusoid environment was expected to show some change in the transmission loss for the source spectrum. However, Fig. 11 shows that the single sinusoid with a magnitude of 10 m/s has negligible effects on the short-range acoustic propagation. Both the CW and BB plots are nearly identical to the RI environment.

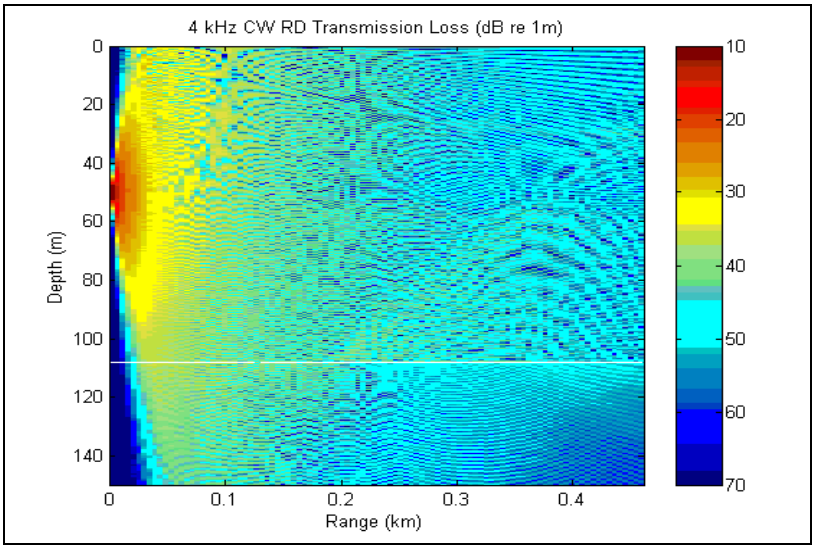

(a)

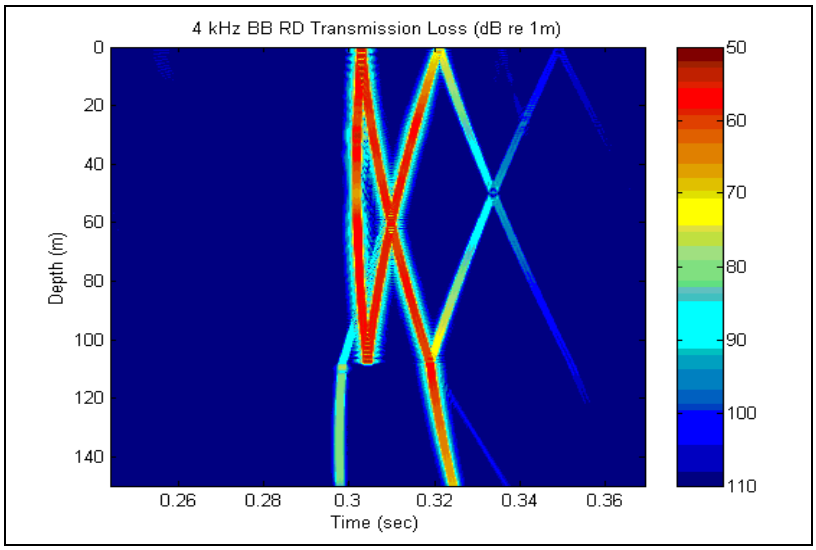

(b)

Figure 11. Range-Dependent Single Sinusoid Transmission Loss (a) 4 kHz CW signal (b) 4 kHz 2 msec Bb pulse

The range-dependent single sinusoid also produced negligible changes to the propagation for the 16 kHz source. Both the BB and the CW 16 kHz signal are nearly identical to the range-independent case; these simple, sinusoidal perturbations do not seem to effect this short-range acoustic propagation.

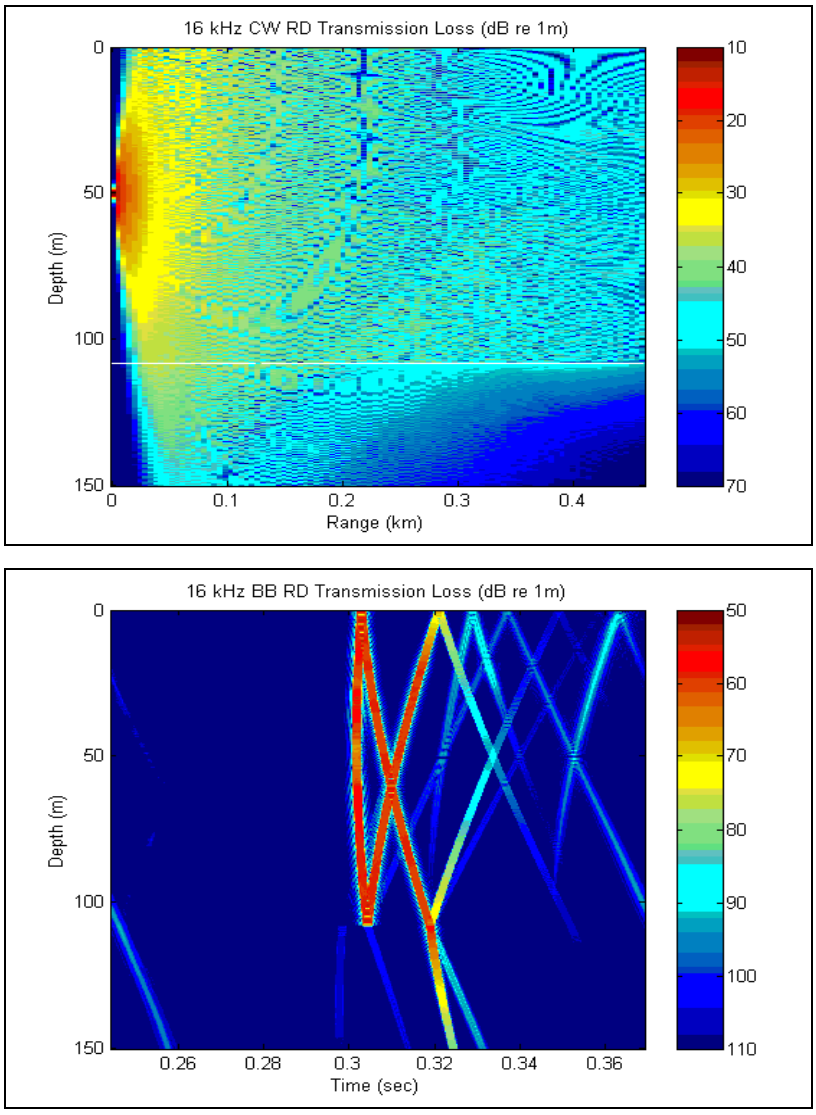

Figure 12. Range-Dependent Single Sinusoid Transmission Loss (a) 16 kHz CW signal (b) 16 kHz 2 msec BB pulse

3. Range-Dependent (RD) Multiple Sinusoids

The multiple sinusoid environment discussed in Section III is now analyzed in an attempt to inject some variability into the propagation. Two different magnitudes of the perturbation scale were used during the model runs and the results for the BB 4 kHz source are shown below in Fig. 13. Even with this more complicated environment, it appears that there is again no change in transmission loss from the RI and RD single sinusoid environments for this short-range propagation. The arrival is crisp with no signal distortion present even with a sound speed fluctuation magnitude as high as 10 m/s.

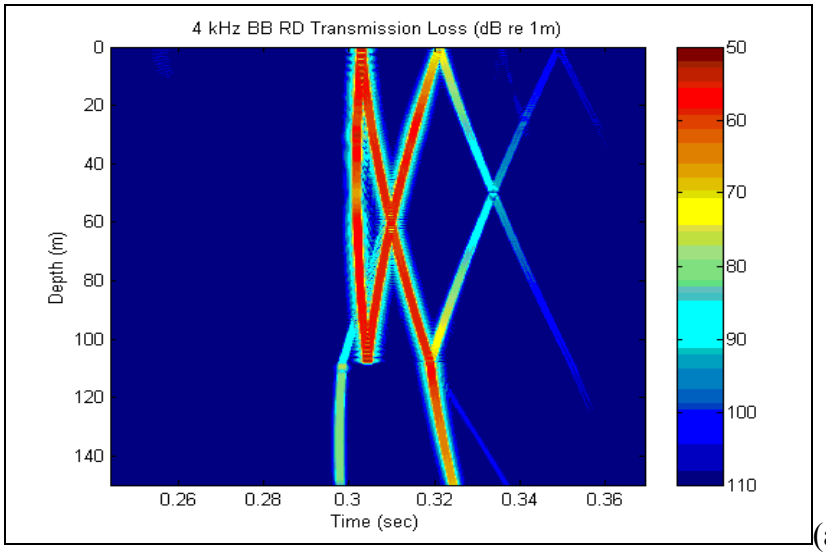

(a)

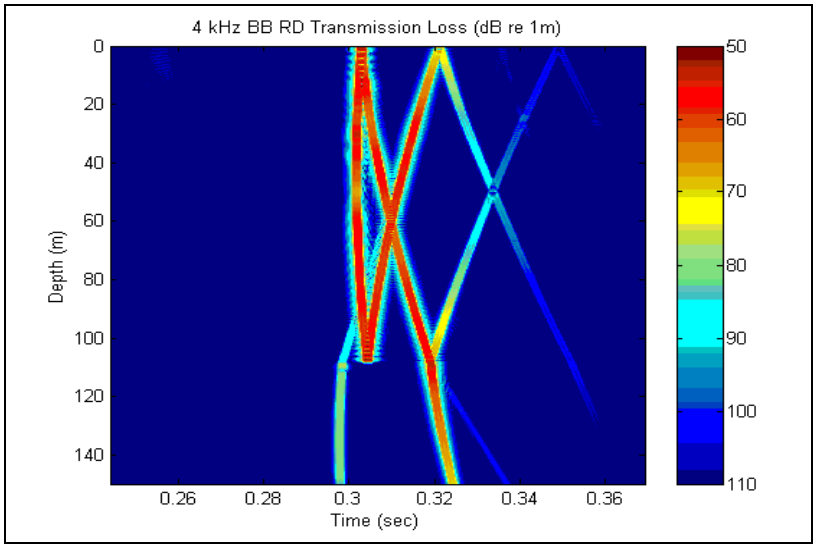

(b)

Figure 13. 4 kHz Range-Dependent Multiple Sinusoids Transmission Loss w/ magnitude (a) 2 m/s, (b) 10 m/s

Results were also computed for the BB 16 kHz source, as displayed in Fig. 14. Similar conclusions may be drawn that the multiple sinusoid perturbation appears to have negligible affect on the propagation over this short range.

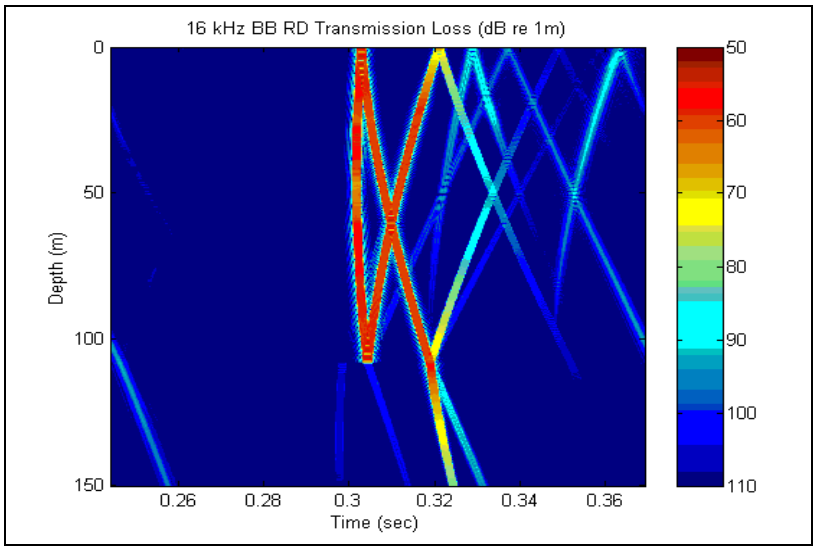

(a)

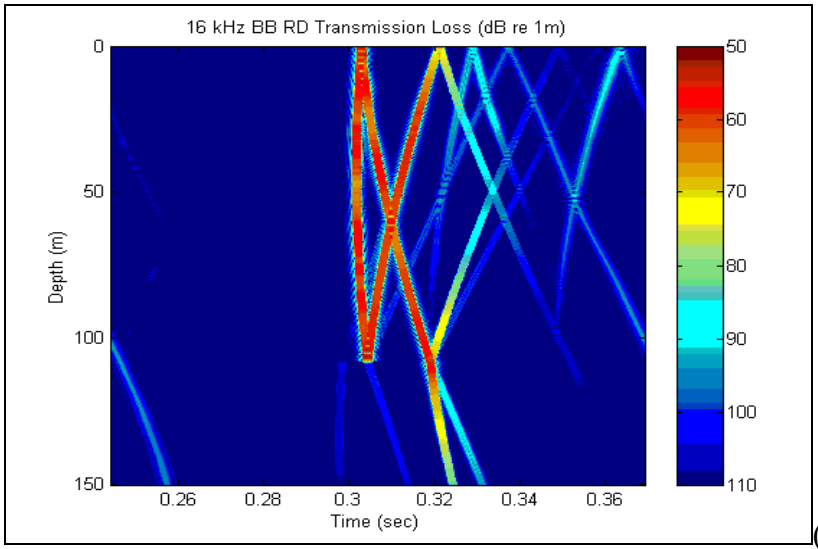

(b)

Figure 14. 16 kHz BB Range-Dependent Multiple Sinusoids w/ rms Magnitudes (a) 2 m/s, (b) 10 m/s

In order to test the validity of the model in the presence of the multiple sinusoid perturbations, the 4 kHz source responses were recomputed out to a range of 5 km. The results from the RI and multiple sinusoid RD calculations for the 4 kHz CW source are presented in Fig. 15. It is clear that the perturbation does impact the propagation at larger ranges.

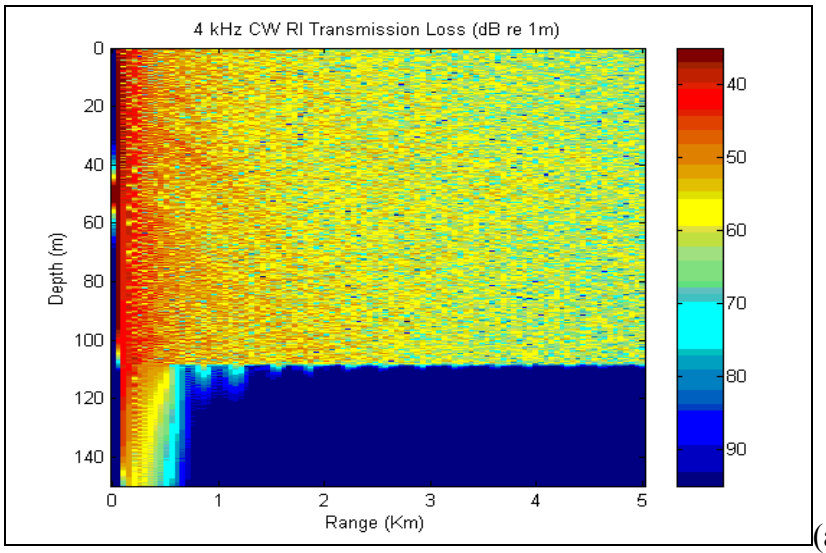

(a)

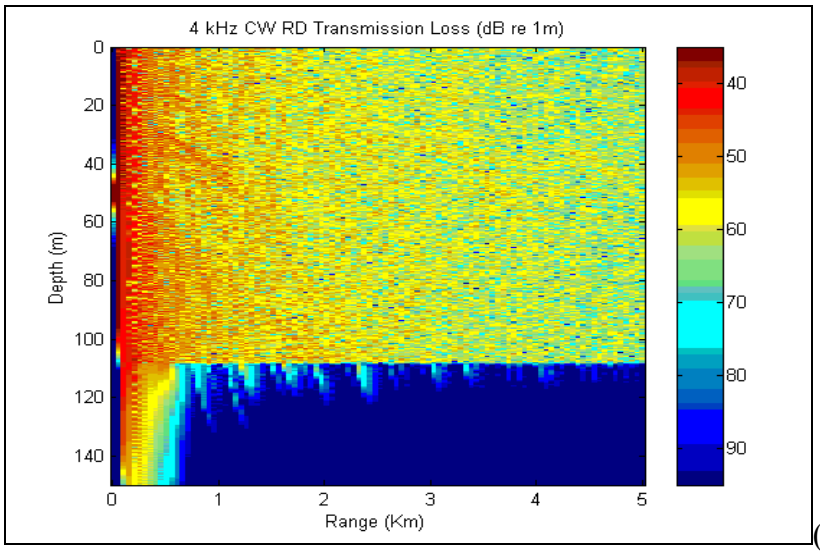

(b)

Figure 15. 4 kHz CW Signal 5 km Transmission Loss (a) RI, (b) RD Multiple Sinusoid

Figure 16 shows the corresponding results for the 4 kHz BB source received at the maximum range of 5 km. Again, the impact on the arrival structure at this range is evident. Thus, the model appears to be working properly, and the conclusion may be made that such simple sinusoidal perturbations, even combinations of multiple length scales, do not impact the short range (~0.5 km) propagation.

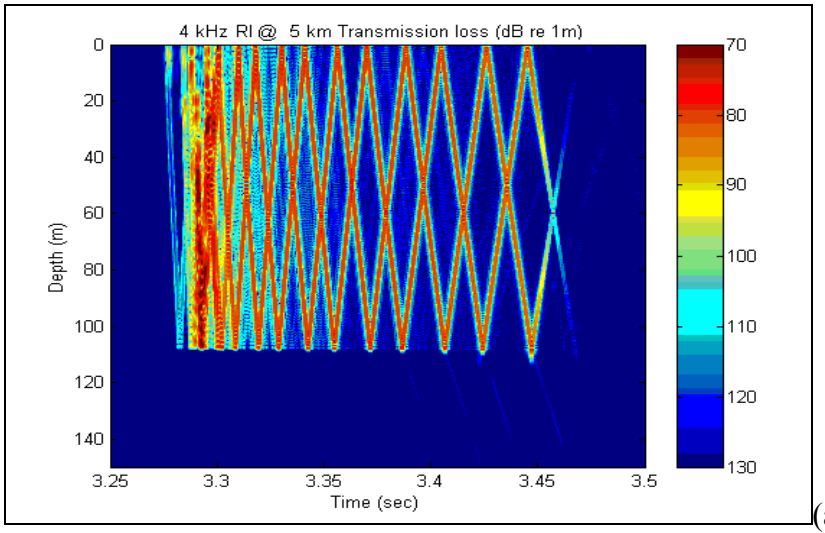

(a)

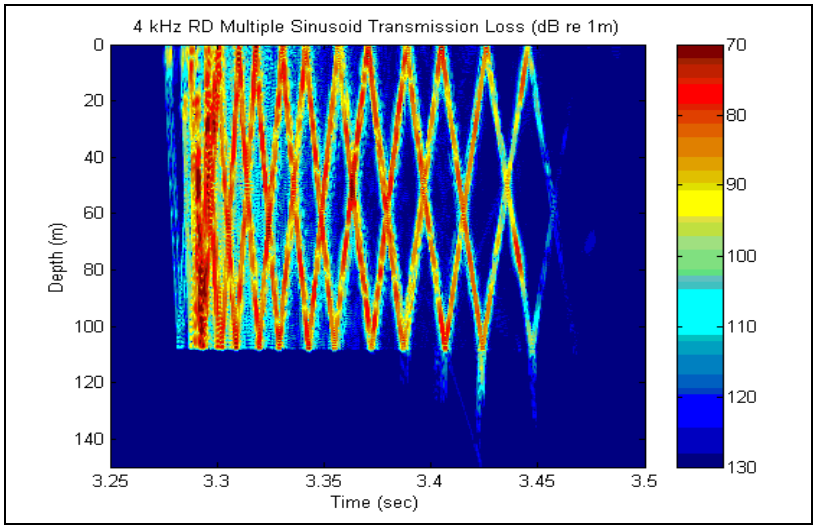

(b)

Figure 16. 4 kHz 2 msec BB pulse, 5 km Transmission Loss (a) RI, (b) RD Multiple Sinusoid

4. Range-Dependent (RD) Turbulent Perturbations

From the previous analysis, it is clear that sinusoidal perturbations on the length scale of typical, linear internal waves do not significantly affect the propagation structure over short ranges to negatively impact vertical coherence. The type of perturbation needed to create any level of decorrelation must then be on the scale of turbulent structure in the water column. The final part of this analysis then employs the spectral scale model of small-scale random perturbations defined in Section II.

Using an rms perturbation value of 2.5 m/s, the results displayed in Fig. 17 were computed for the 4 kHz CW source. Although some modal interference structure is still observable, it is significantly degraded. There also appear to be some caustic, ray-like structures of high intensity refracting through the water column. These are presumably the result of energy focusing near the source in micro channels set up by the turbulent perturbations

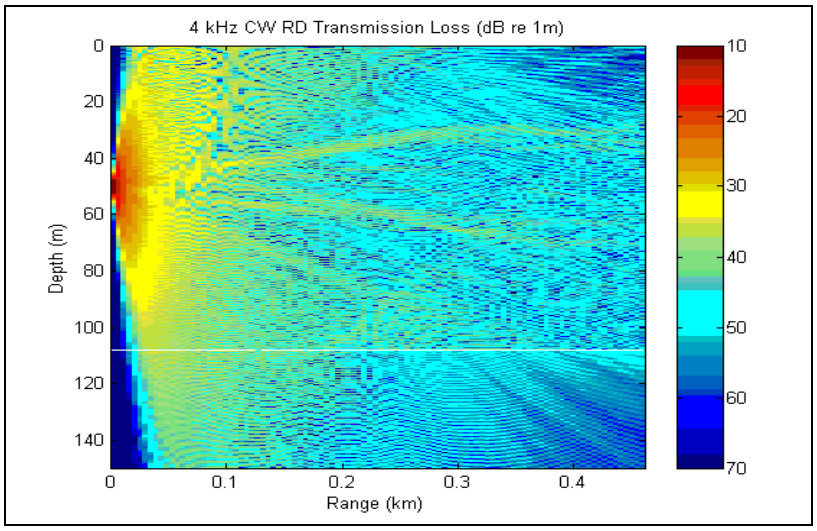

Figure 17. 4 kHz CW Range-Dependent Turbulent Perturbations w/ 2.5 m/s rms Magnitude

The 4 kHz BB model runs consisted of three different rms magnitudes of perturbations: 1 m/s, 2.5 m/s and 5 m/s. The transmission loss for each of these rms magnitudes is shown in Fig. 18. With only a 1 m/s rms turbulent fluctuation magnitude, the 4 kHz BB signal began to show a slight arrival distortion, which should produce vertical decorrelation. As the rms magnitude of the fluctuations increased, the arrival distortion increased as well, as expected.

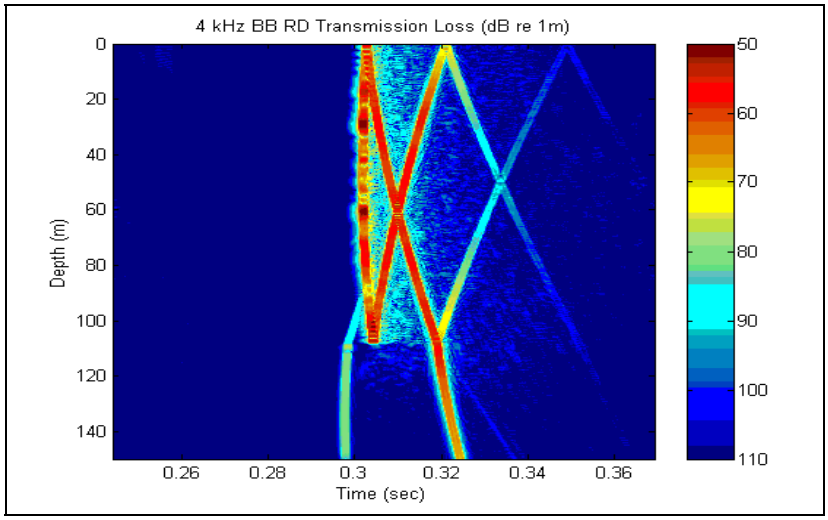

(a)

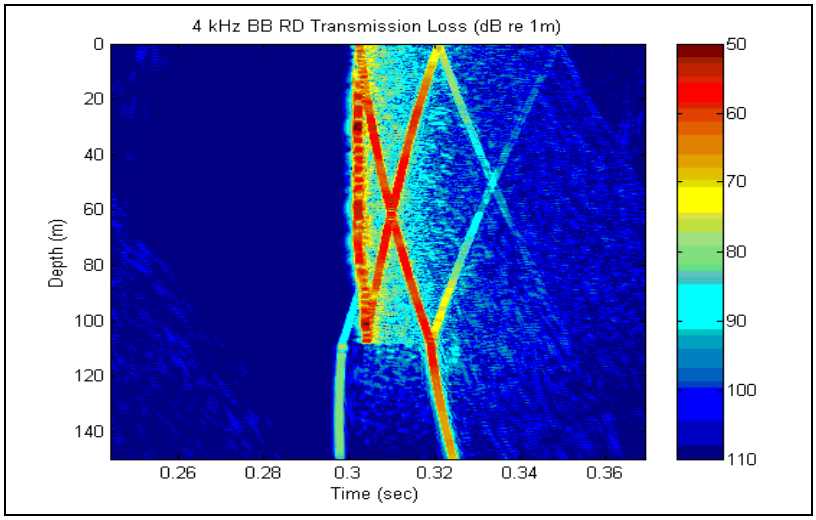

(b)

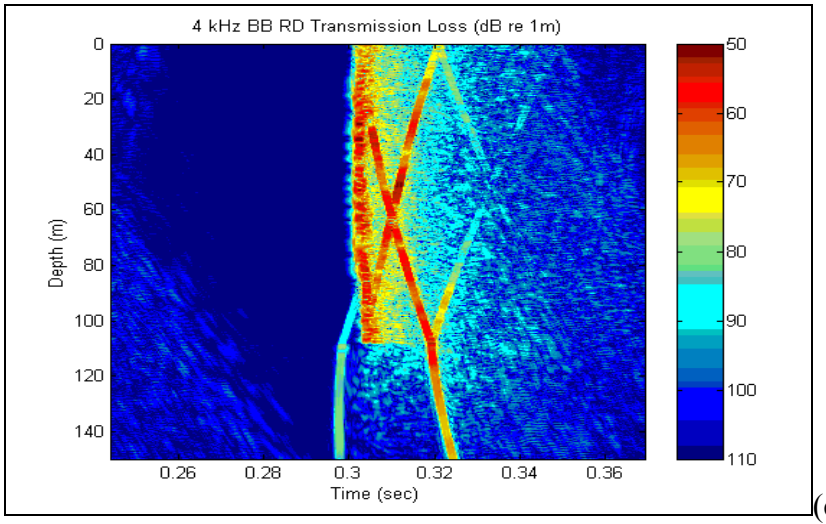

(c)

Figure 18. 4 kHz BB Range-Dependent Turbulent Perturbations with rms Magnitudes, (a) 1 m/s, (b) 2.5 m/s, and (c) 5 m/s

This range-dependent turbulent environment was then used to show the effects on higher frequencies by transmitting the 16 kHz BB source. The 16 kHz BB pulse model runs consisted of three different rms magnitudes of perturbations: 0.5m/s, 0.75 m/s and 1 m/s. The transmission loss arrival structure for each of these rms magnitudes is shown in Fig. 19. Apparent from the plots, the onset of signal distortion appears quite rapidly at the higher frequency. With only a 0.5 m/s rms turbulent fluctuation magnitude, the 16 kHz BB signal began to show a slight arrival distortion. The results suggest that the 16 kHz frequency undergoes more attenuation in this environment. Similar to the 4 kHz source, as the magnitude of the fluctuations increased, the arrival distortion increased as well. From these observations, it can be concluded that there is dependence between the minimal magnitude of fluctuation required to cause signal distortion and the frequency of the source. Since it is apparent that these fluctuations affect the signal propagation, it is expected that the vertical spatial correlation will be affected as well.

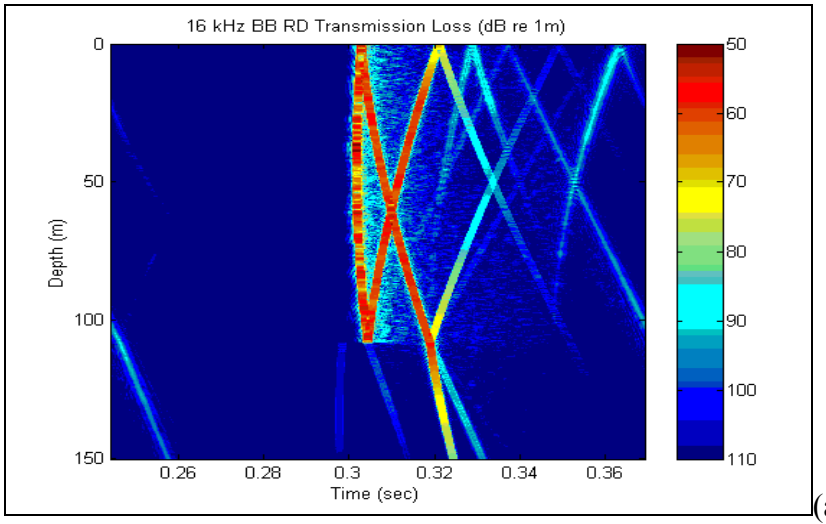

(a)

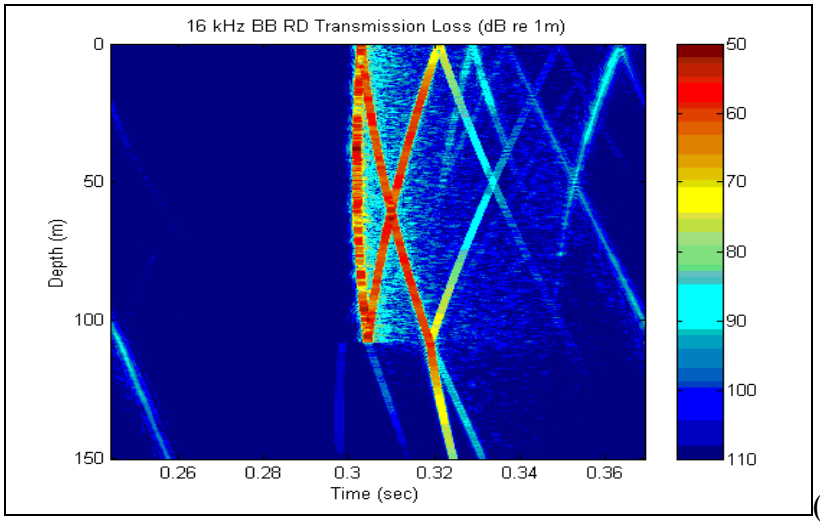

(b)

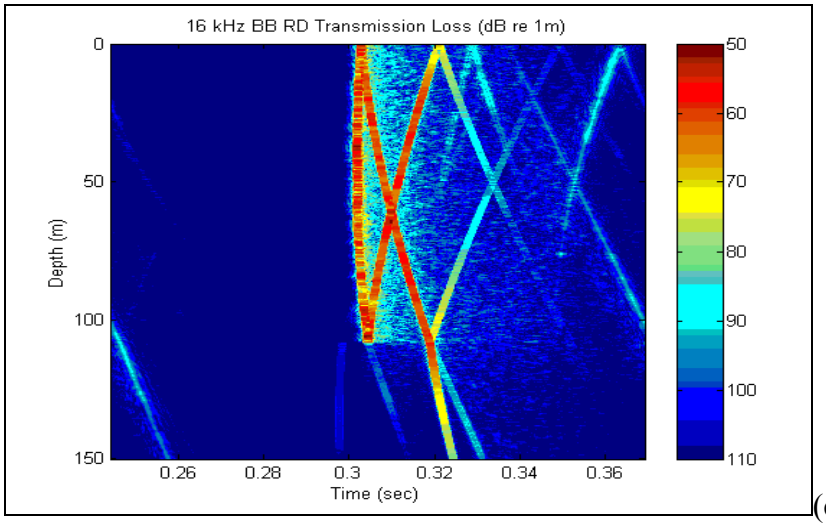

(c)

Figure 19. 16 kHz BB Pulse Range-Dependent Turbulent Perturbations with rms Magnitudes, 0.5 m/s, (b) 0.75 m/s, and (c) 1 m/s

B. POST PROCESSING 2 - DIRECT PATH EXTRACTION

With the MMPE arrival structures properly determined, it is now necessary to extract the data at the appropriate depths associated with the elements of the upper and lower arrays. Since our interest is the vertical spatial coherence and its relationship with the water column variability, the direct water-bourne propagation path will need to be extracted at each of the element depths. During the ASIAEX experiment, two different source depths were transmitted, 25 and 50 meters. Both these source depths were run in the model and the resulting arrival trace plots were similar for all four frequencies. In general the first three peaks received were the direct path, surface bounce and bottom bounce, respectfully. However, with the source at 25 meters the direct path signal could not be isolated in the upper array due to the interference with the surface bounce arrival, see Fig. 20.

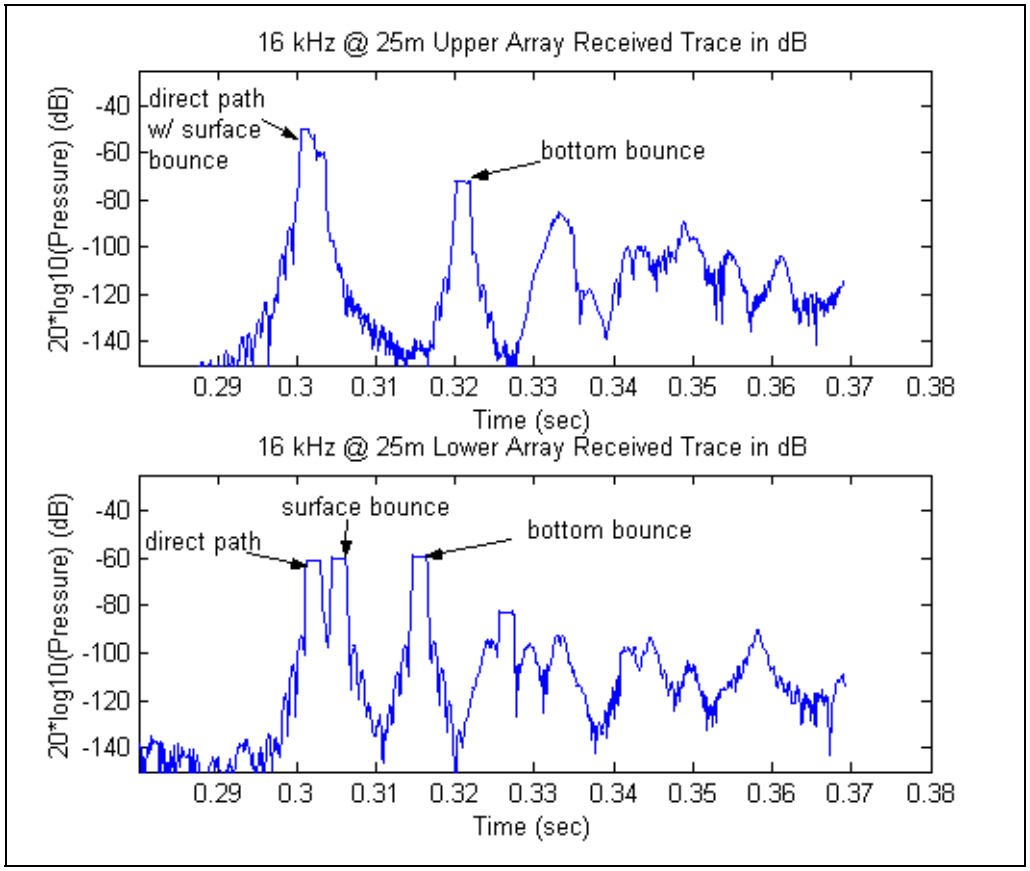

Figure 20. 16 kHz Source @25m Upper and Lower Array Received Pressure Trace in dB.

Figure 21 shows the source at 50 meters for the center frequency of 16kHz. Clearly the direct path signal can be extracted from both the upper and lower array for our analysis. This ability is critical, since any decorrelation associated with interaction with the surface or bottom interfaces would contribute to false results. A source depth of 50 meters will be used for the remainder of the experiment.

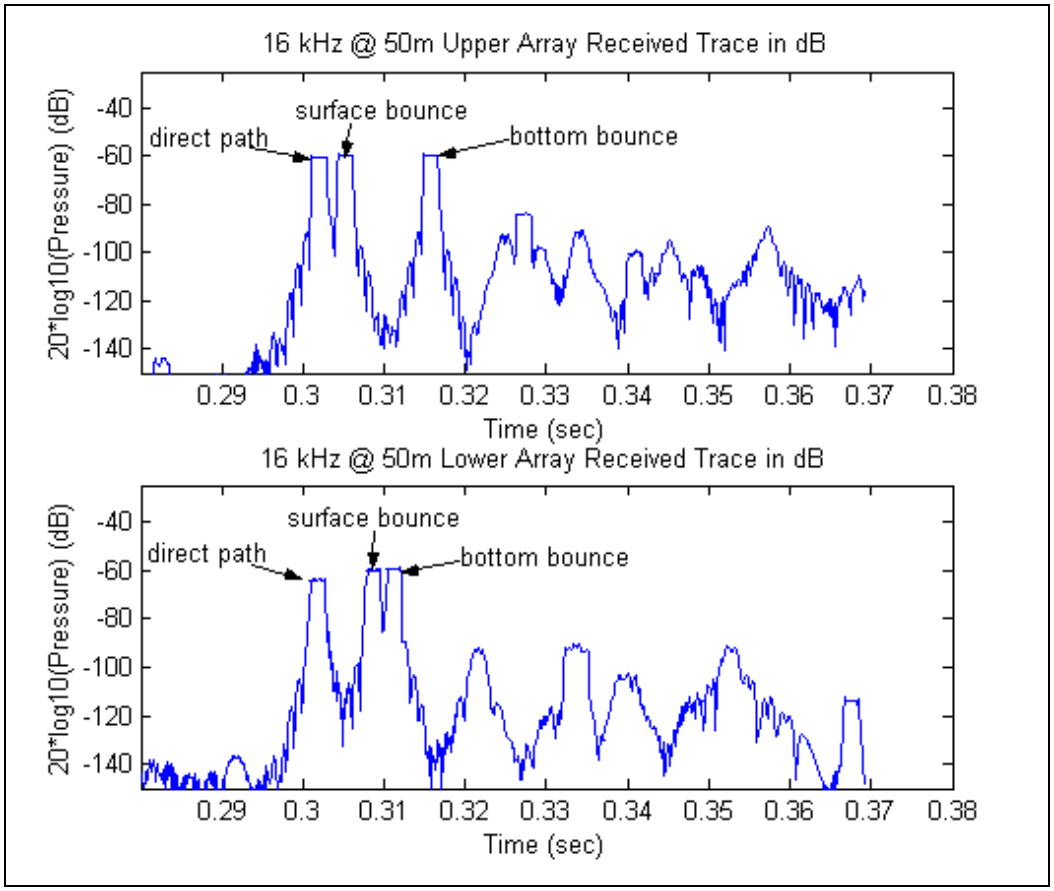

Figure 21. 16 kHz Source @50m Upper and Lower Array Received Pressure Trace in dB.

To isolate the direct path signal, a threshold was placed on the signal similar to the detection threshold process used by submarines to isolate a signal over the noise. 'The words 'detection threshold' imply two of the most important aspects involved in extracting a signal from the background in which it is embedded: (1) the function of detection itself, and (2) the existence of a threshold somewhere near the output of the receiving system.'[8] The isolation of the direct path signal in this experiment is a process

much simpler than a typical detection threshold. An isolation threshold was placed on our received arrival trace to filter the signal from the noise, as depicted in Fig 22.

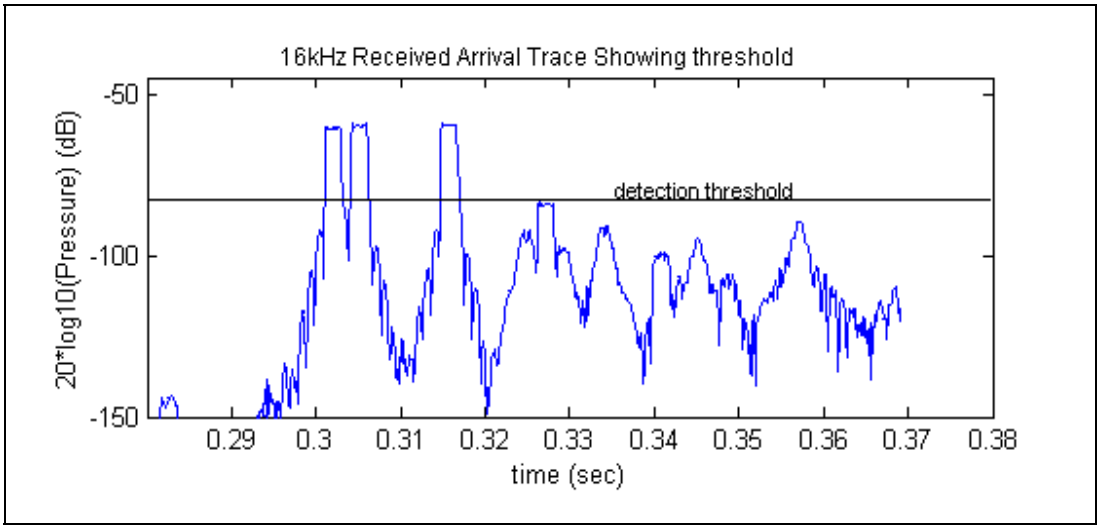

Figure 22. 16 kHz Received Arrival Trace Showing Isolation Threshold

Once the three arrival peaks were isolated from background noise, the minimum index of the direct path signal was found by determining the first point that exceeds the threshold. Similarly the maximum index of the direct path signal was found by determining the subsequent point that falls back below the threshold. The center index of the peak was found by determining the midpoint. Now that the direct path peak is isolated, a filter was used to properly size and smooth the signal. The filter consisted of a 2 msec rectangular window; along with a 1 msec Hanning window split into two segments placed on each end of the rectangular window. This shape of this filter was already discussed in detail in Section II. The resulting pressure signal was then padded to yield the correct array length for further analysis in the vertical spatial correlation section to follow. Figure 23 shows both the isolated three-peak signal and the padded direct path signal used for correlation.

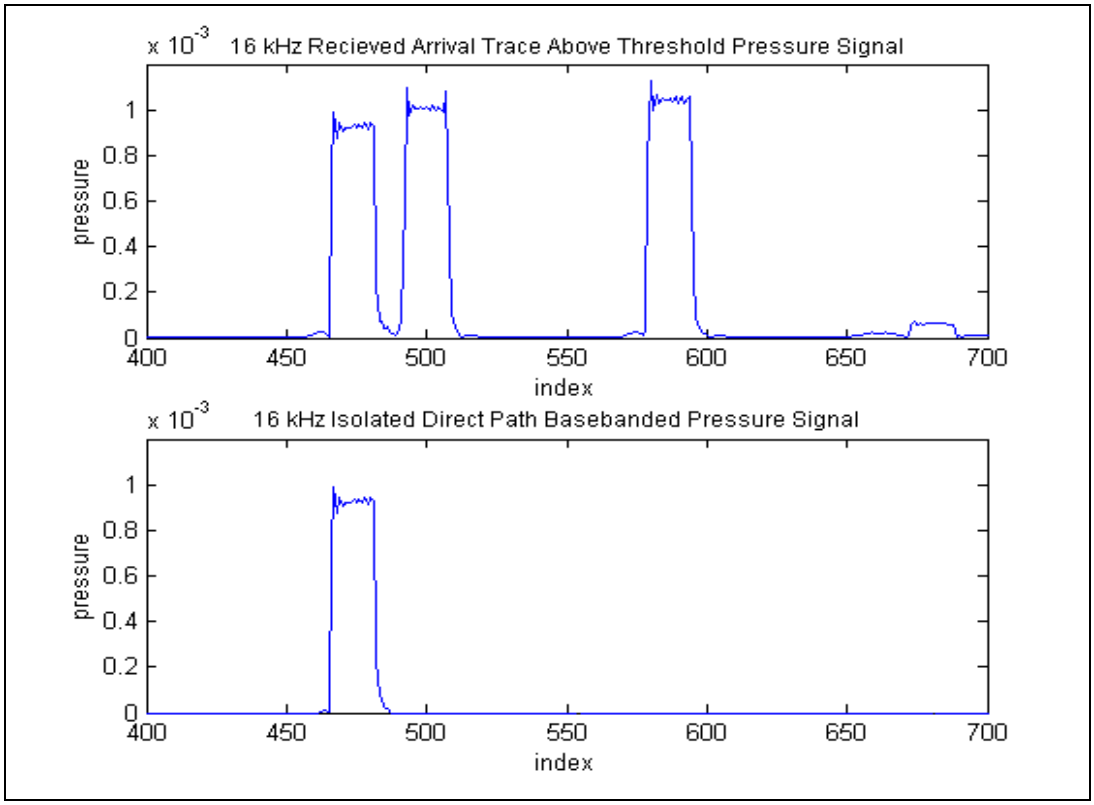

Figure 23. 16kHz Received Arrival Trace Above Threshold Pressure Signal and the Isolated Direct Path Basebanded Pressure Signal.

C. POST PROCESSING 3 - VERTICAL SPATIAL CORRELATION

A useful measure of the degradation of a received waveform is known as coherence. Coherence is the degree of signal waveform similarity between any two spatially separated receiving elements.[8] The coherence of a waveform is found using the cross-correlation between the two signals. This analysis examines a normalized cross-correlation using the received pressure in the time domain. This function is, in general, complex, so the absolute value is reported in this analysis. The results are then defined as the maximum of the function

$$C_{p1,p2}(\tau) = e^{-i2\pi f_c \tau} \frac{\int p_1'(T)\, p_2'^{*}(T-\tau)dT}{\sqrt{\int |p_1'(T)|^2\, dT \int |p_2'(T)|^2\, dT}}, \tag{48}$$

where p_1' & $p_2'^{*}$ are the first base-banded pressure signal and the complex conjugate of the second base-banded pressure signal.

1. Range-Independent and Single Sinusoid Range-Dependent Correlation

The initial coherence comparisons were analysed with the 4 kHz and 16 kHz model runs. Due to the relatively short-range propagation, it is expected that the range-independent (RI) vertical correlation will be nearly perfect with possibly a notable decorrelation using the 10 (m/s) single sinusoid, range-dependent (RD) environment. The vertical correlation results, as seen in Figs 24 and 25, provided nearly perfect coherence from the RI environment as well as the single sinusoid RD environment.

The high level of correlation of the RD data (as high as the RI data) is perhaps not completely surprising. In order to produce significant decorrelation across the relatively short vertical arrays would require vertical sound speed perturbations on roughly the same scale. However, the vertical structure of the sinusoidal perturbations is quite smooth. With both the 4 kHz and 16 kHz showing no decorrelation, we omitted duplicating results by not showing the 8 kHz and 20 kHz frequencies

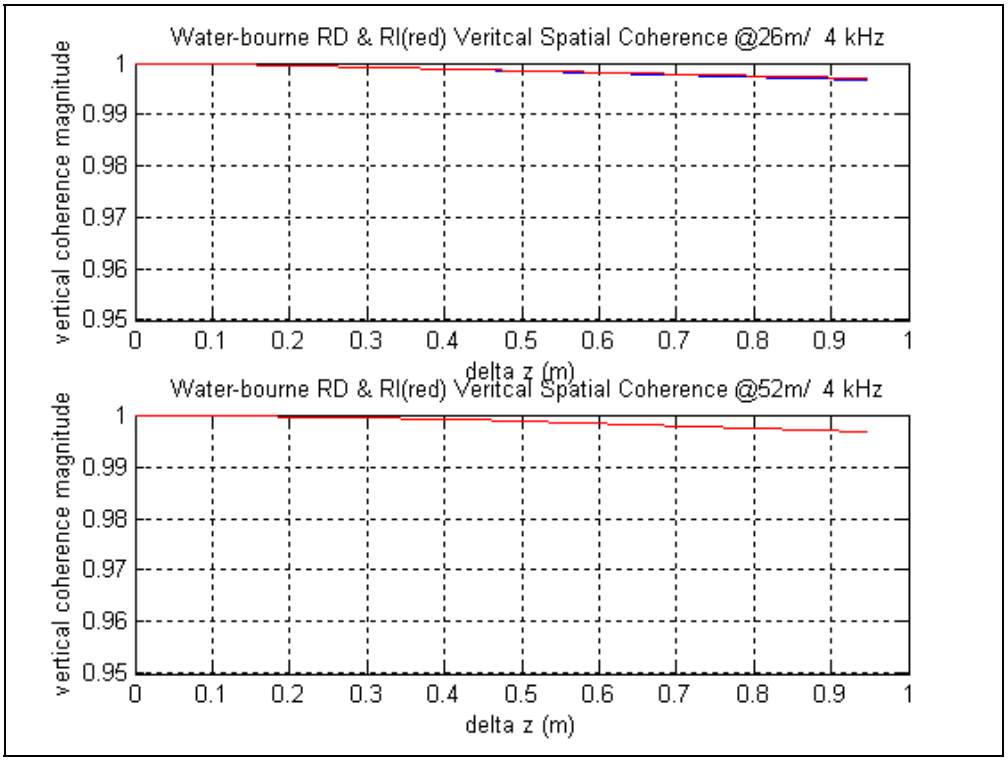

Figure 24. 4 kHz Vertical Spatial Coherence for Range-Independent and Single-Sinusoid Range-Dependent Environments for the Upper and Lower Arrays.

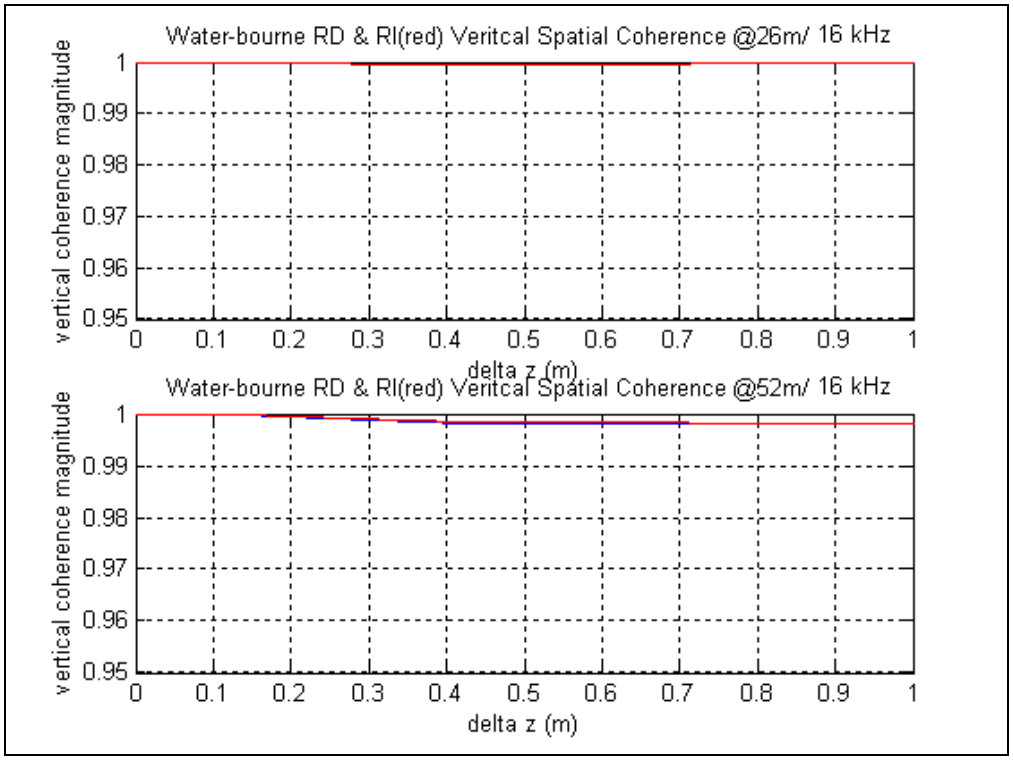

Figure 25. 16 kHz Vertical Spatial Coherence for Range-Independent and Single-Sinusoid Range-Dependent Environments for the Upper and Lower Arrays.

2. Multiple Sinusoid Range-Dependent Correlation

To test the previous observation with a slightly more complicated structure, the multiple sinusoid environment discussed in Section III was analysed. The vertical spatial correlation was computed and the results are shown below. During this analysis the RI correlation lines are included for comparison. In addition to the RI data, two different magnitudes are plotted together, in an attempt to show some decorrelation from a multiple sinusoid environment. The results can be seen in Figs 26 and 27.

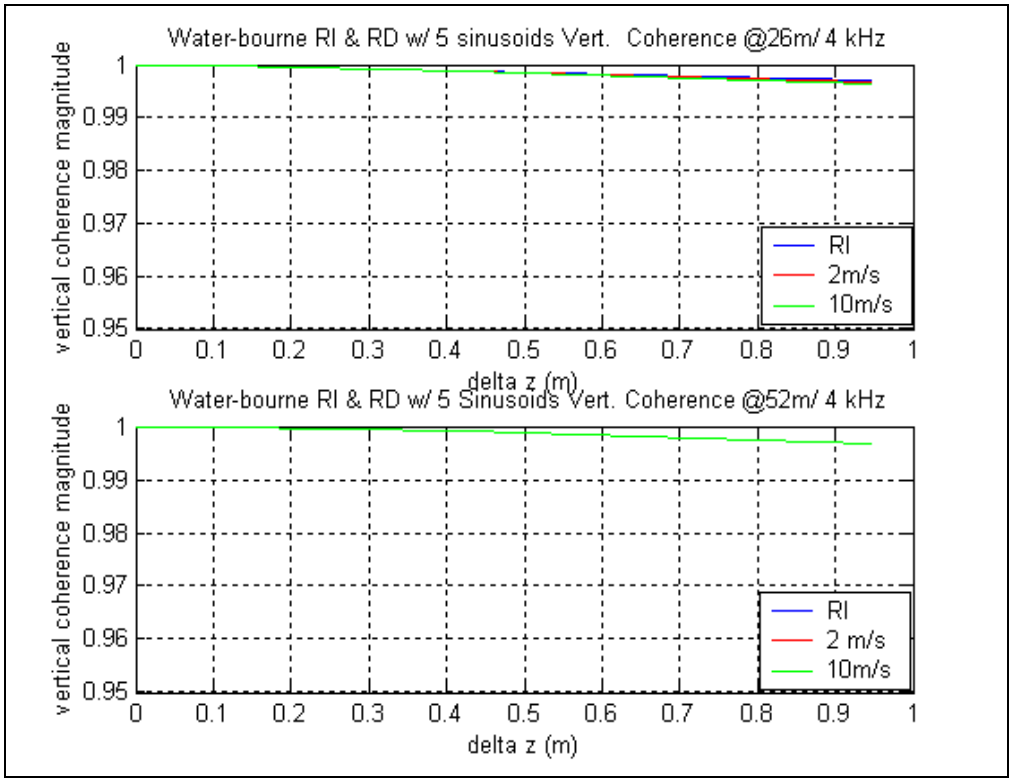

Figure 26. 4 kHz Vertical Spatial Coherence for Range-Independent and Multiple-Sinusoid Range-Dependent Environments for the Upper and Lower Arrays

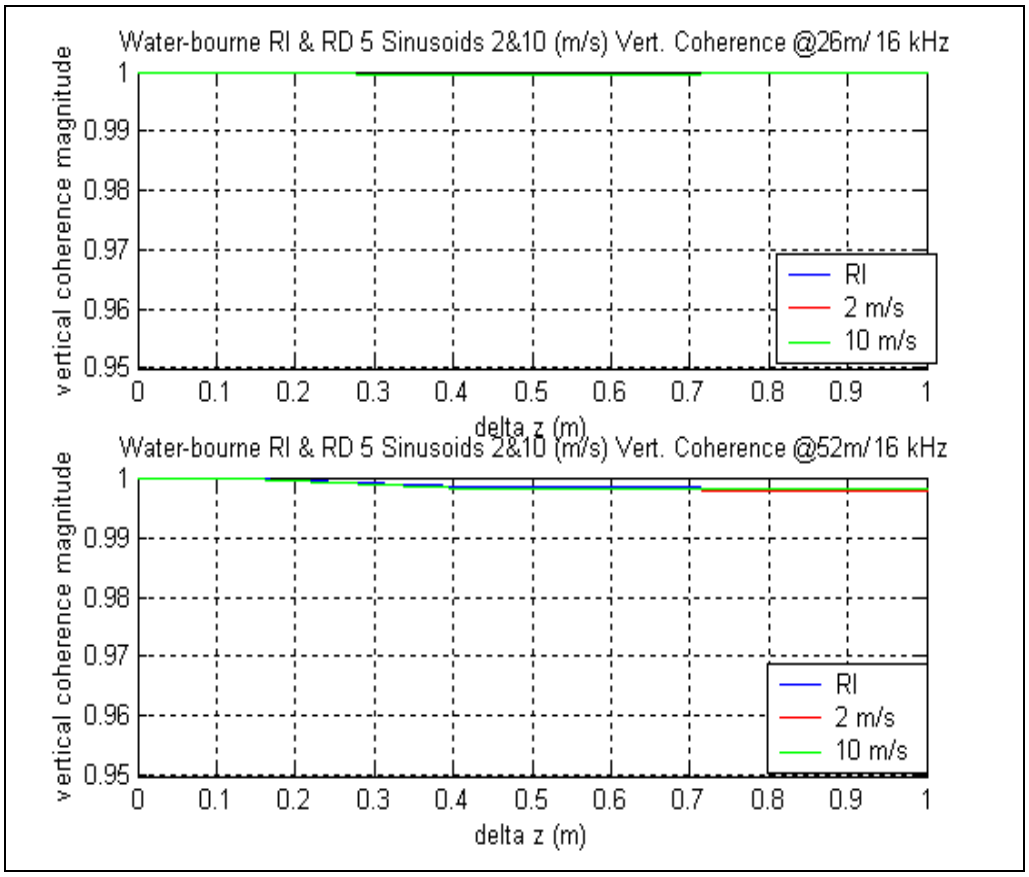

Figure 27. 16kHz Vertical Spatial Coherence for Range-Independent and Multiple-Sinusoid Range-Dependent Environments for the Upper and Lower Arrays

Similar to the single sinusoid environment, the multiple sinusoid environment also produced no additional decorrelation to the direct water-bourne propagation path. The explanation for this lack of decorrelation is the same as before. With both the 4kHz and 16kHz showing no decorrelation, the results of the 8 kHz and 20kHz frequencies are omitted.

3. Turbulent Perturbation Range-Dependent Correlation

The previous analysis suggests that small-scale fluctuations in the vertical direction are needed to introduce any significant decorrelation across the arrays. The random perturbations defined for this environment may then be expected to produce such decorrelation. The results of this analysis confirm these expectations.

During this analysis the RI correlation line was left on the figures for comparison. In addition to the RI data, several different turbulent data were computed using various magnitudes and the results were plotted together in the following figures. From these figures it is observed that the turbulent 2-D variability spectrum introduced into the environment is linked directly to lower correlation values.

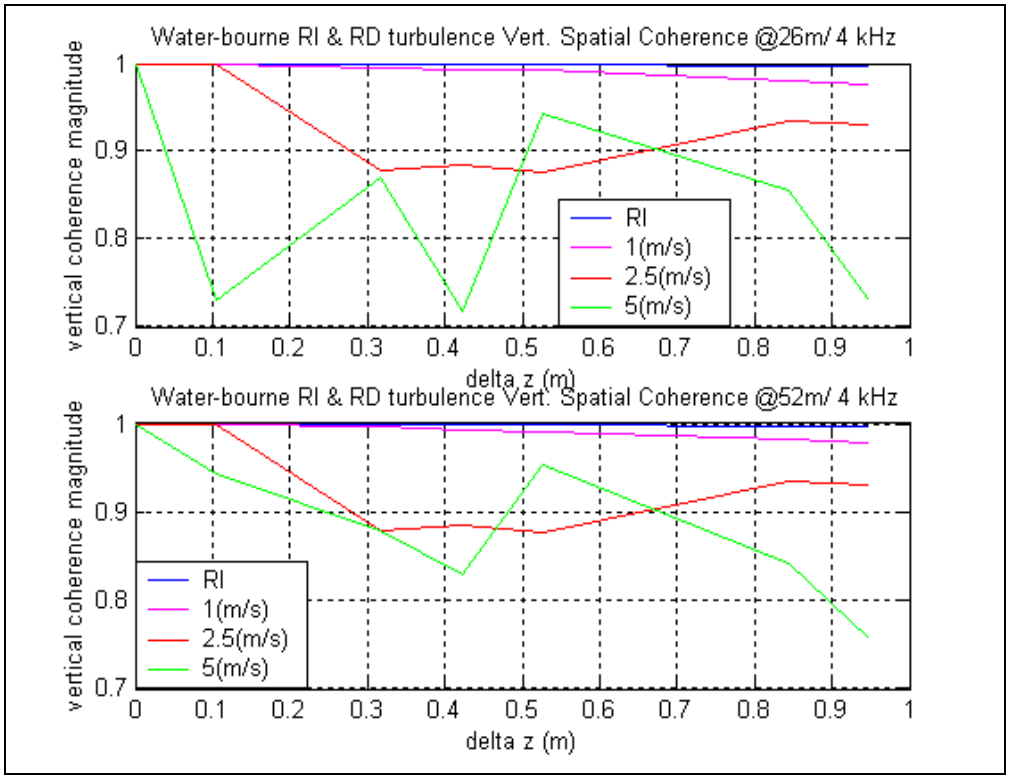

Figure 28. 4kHz Vertical Spatial Coherence for Range-Independent and Turbulent Perturbation Range-Dependent Environments for the Upper and Lower Arrays

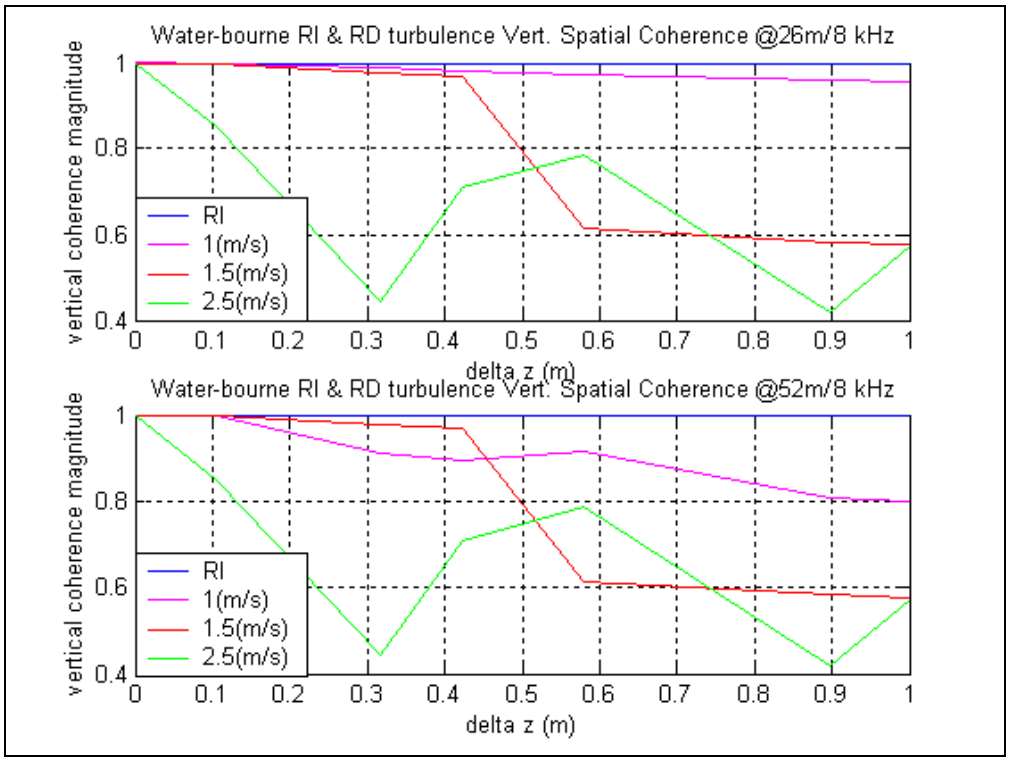

Figure 29. 8kHz Vertical Spatial Coherence for Range-Independent and Turbulent Perturbation Range-Dependent Environments for the Upper and Lower Arrays

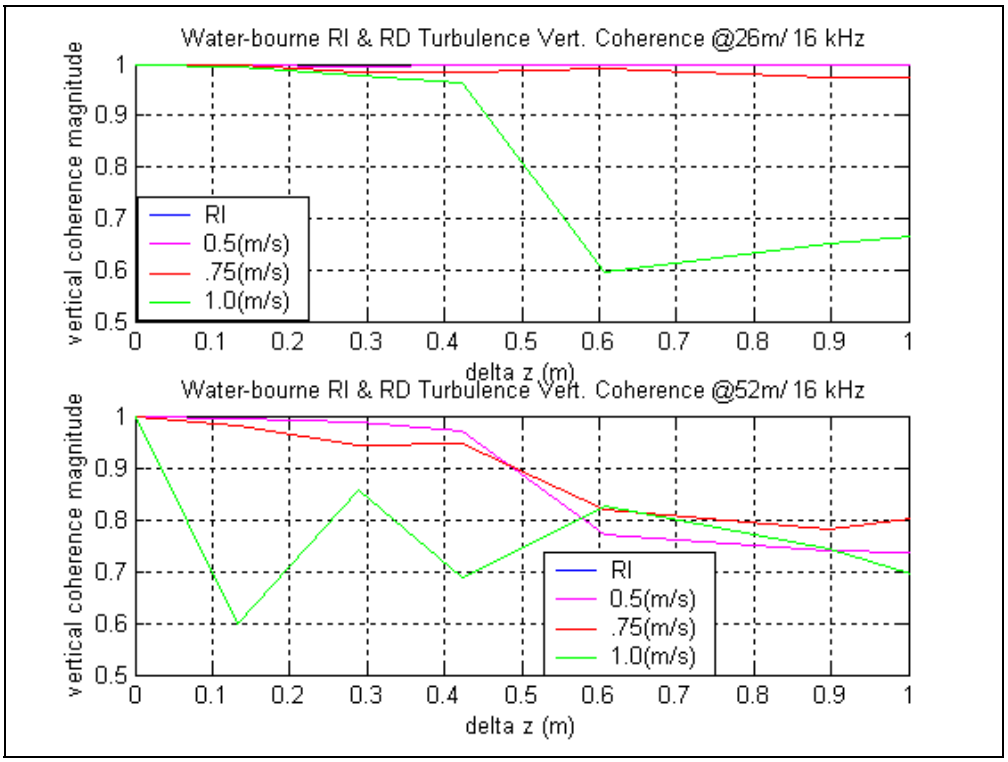

Figure 30. 16kHz Vertical Spatial Coherence for Range-Independent and Turbulent

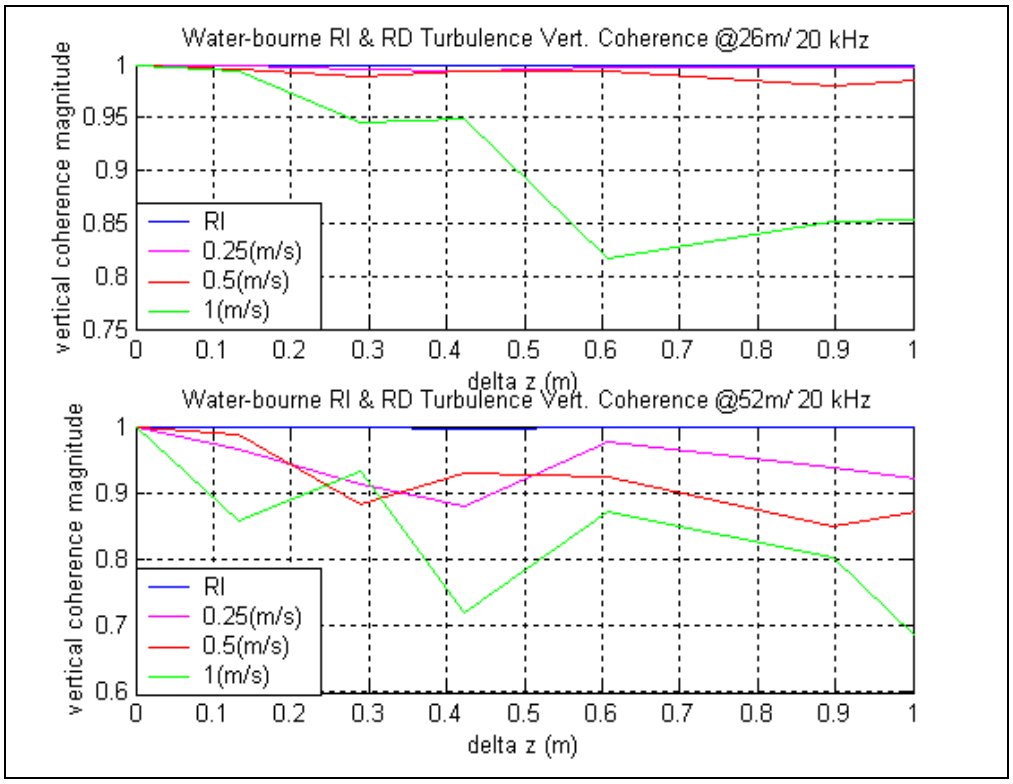

Figure 31. 20kHz Vertical Spatial Coherence for Range-Independent and Turbulent Perturbation Range-Dependent Environments for the Upper and Lower Arrays

The onset of decorrelation appears rather rapidly with increasing magnitude of the turbulent perturbations. The results also suggest that the magnitude of turbulent fluctuations needed for the onset of decorrelation is frequency dependent. This is not surprising, as we would expect decorrelation effects due to the acoustic wavelength to be on the order of the typical scale size of sound speed granularity. For a transmitted signal of 4 kHz, the magnitude of the perturbations is approximately 2.5 m/s at the onset of decorrelation. At the higher transmitted frequency of 20 kHz, the onset of decorrelation was already evident at a magnitude of 0.25 m/s. The lower frequency appears to require 10 times more variability to produce an equivalent decorrelation as the higher frequency.

THIS PAGE INTENTIONALLY LEFT BLANK

V. SUMMARY

A. CONCLUSIONS

The focus of this thesis was relatively short-range (~500m) acoustic propagation of frequencies of O(10) kHz of the direct water-bourne propagation path through variable oceanographic conditions. Numerical predictions were made using modeled environmental conditions and the same array geometry used during the ASIAEX, East China Sea experiment. In order to simulate shallow water variability, three different range-dependent perturbations were individually introduced: a perturbation consistent with a linear internal wave with range dependence based on a single sinusoid; a perturbation consistent with a group of linear internal waves based on the combination of multiple sinusoidal fluctuations in range; and a field of random perturbations based on a power law spectrum intended to generate turbulent-like structure. A range-independent environment was also used in the analysis for comparison. Several different analyses were conducted on each environment in order to determine the influence of shallow-water variability on acoustic propagation.

Transmission loss analysis was done to illustrate the potential effects of shallow water variability on the direct water-bourne propagation path. The computation of TL was used to show the signal loss and the arrival structure from a source at both 25 m and 50 m. From the arrival structure using the 25-meter source, it was evident that the direct propagation path could only be isolated within the signal received at the lower array cluster. In order to examine model data at both sub-array depths, the 50-meter source was used throughout the analysis. The 4kHz, 8kHz, 16kHz and 20kHz center frequency 2 msec pulses were transmitted through each of these simulated shallow water environments. The arrival structure was computed for both the CW center frequency and the broadband 2 msec pulse, allowing for quick examination of the environmental propagation losses.

The first set of perturbations examined were those associated with the sinusoidal fluctuations intended to illustrate the effects of linear internal waves. All the frequencies used resulted in a crisp arrival with no signal distortion present, even with the multiple

sinusoid environment with a peak magnitude as high as 10 m/s. It can then be concluded that at short ranges (~0.5 km), simple sinusoidal perturbations and even combinations of multiple length scales have negligible affect on the propagation, regardless of the frequency. Longer-range test results did exhibit noticeable effects, however, indicating that the model was working correctly.

The analysis then focused on the influence of the turbulent-like, random perturbations. In this case, the appearance of signal degradation was evident. The CW TL structure showed noticeable breakdown in the modal interference structure with some caustic, ray-like structures of high intensity refracting through the water column. These are presumably the result of energy focusing near the source in micro channels set up by the turbulent perturbations. The 2 msec broadband model runs were conducted using several different rms magnitudes of perturbations. It can be concluded that as the magnitude of the fluctuations increased, the arrival distortion increased as well. In addition, the onset of signal distortion appears at lower rms perturbation values at the higher frequencies. The 16 kHz signal required a smaller magnitude of sound speed fluctuation to create the same signal distortion as the 4 kHz signal with a higher magnitude. Comparing Figures 18 and 19, it can be concluded that there is a relationship between the minimal magnitude of fluctuation required to cause a specific amount of signal distortion and the frequency of the source.

As a measure of signal distortion, this thesis examined the normalized cross-correlation of the received pressure in the time domain. Due to the relatively short propagation range and the small vertical arrays, the vertical correlation was nearly perfect for the range-independent and single/multiple sinusoidal range-dependent environments. The sinusoidal fluctuations, similar to internal waves, have range-dependent fluctuations of varying range scale, but are relatively smooth in depth.

The random perturbation environment, however, provided the necessary vertical scale variability in the sound speed to cause significant decorrelation. Correlation results were computed for the 4 kHz, 8 kHz, 16 kHz and 20 kHz 2 msec pulses. For all four frequencies, there was a direct relationship between the magnitude of decorrelation and the rms magnitude of the turbulent sound speed fluctuation introduced into the water

column. As the rms magnitude of turbulent fluctuations increased, the correlation of the signal decreased. Similar to the transmission loss conclusions, the onset of decorrelation also appears quite rapidly at higher frequencies. Furthermore, lower frequencies appear to require 10 times more variability to produce the equivalent decorrelation as the higher frequency. Higher frequencies result in smaller acoustic wavelengths, which interact with more of the turbulent fine-scale structure. These results can help future forecasting abilities by noting that, the magnitude scale of turbulent volume fluctuations can be estimated by examining the onset of significant vertical decorrelation as a function of frequency

B. RECOMMENDATIONS AND FUTURE WORK

True of most research, several areas were left which require additional investigation for future students. The first of which is the incorporation of a more realistic ocean turbulence environment into the MMPE program. In this thesis, a simple sinusoid was used to simulated internal waves and turbulent-like perturbations were introduced from a 2-D variability spectrum derived for use in an ocean floor. Noting these models of water column turbulence variability are very generic, they allow a first-glimpse analysis of the potential effects of such fluctuations.

Another area for future research would be the statistical comparison of the vertical spatial correlation to the results from the team at the APL, U of W. The applicable data retrieved from the ASIAEX is currently being analyzed at the U of W. Upon completion of the analysis, a student at the Naval Postgraduate School has already agreed to begin the statistical comparison.

Further analysis would also be beneficial, implementing combinations of variability models. This analysis performed in this thesis was done introducing one type of shallow water variability environment at a time. Since actual littoral conditions possess a combination of variability, perhaps incorporating a sinusoidal fluctuation with a random perturbation would provide a better understanding of the true effects of shallow-water acoustic phenomena.

THIS PAGE INTENTIONALLY LEFT BLANK

LIST OF REFERENCES

1) Coelho, Emanuel. "*Mesoscale Small Scale Oceanic Variability Effects on Underwater Acoustic Signal Propagation*." SACLANT Undersea La Spezia, Italy

2) Dahl, P. *ASIAEX Cruise report,* University of Washington Applied Physics Laboratory 2001.

3) Smith, K.B. "*Convergence, Stability, and Variability of Shallow Water Acoustic Predictions Using a Split-step Fourier Parabolic Equation Model*," *J. Comp. Acoust*., Volume 9, Number 1, September 1999.

4) Tappert, F. D. "*The Parabolic Approximation Method," in Lecture Notes in Physics*, Vol. 70, Wave Propagation and Underwater Acoustics, edited by J. B. Keller and J. S. Papadakis (Springer-Verlag, New York, 1977).

5) Tolstoy, A., Smith, K., Maltsev, N., *SWAM 99 Workshop- An Overview,* J. of Computational Acoustics, Vol.9, No. 1 (2002) 1-16

6) Lee, Boon C. *"Environmental Influence on Shallow Water Bottom Reverberation,*" Master's Thesis, Naval Postgraduate School, Monterey, CA, March 2002

7) Jenson, F.B., Kuperman, W. A., Porter, M. B., Schmidt, '*H. Computational Ocean Acoustics'* (Springer-Verlag New York, Inc. 2000) pp. 11

8) Urick, R.J. '*Principles of Underwater Sound',* Third Edition (McGraw-Hill, Inc., 1993). pp 343-344, 33.

9) Li, L.S. "*Parabolic Equation Modeling of Bottom Interface and Volume Reverberation in Shallow Water*," Master's Thesis, Naval Postgraduate School, Monterey, CA, September 2000.

10) Dahl, P. H. "*ASIAEX, East China Sea, Cruise Report of the Activities of the R/V Melville 29 May to 9 June 2001*," Applied Physics Laboratory, University of Washington, Seattle, WA, July 2001.

11) Hardin, R. H. and Tappert, F. D. "*Applications of the Split-step Fourier Method to the Numerical Solution of Nonlinear and Variable Coefficient Wave Equations*," SIAM Rev. 15, 1973.

THIS PAGE INTENTIONALLY LEFT BLANK

INITIAL DISTRIBUTION LIST

1. Defense Technical Information Center
   Ft. Belvoir, Virginia

2. Dudley Knox Library
   Naval Postgraduate School
   Monterey, California

3. Prof. Kevin B. Smith (Code PH/Sk)
   Department of Physics
   Naval Postgraduate School
   Monterey, California

4. Dr. Jeff Simmen (Code 321OA)
   Office of Naval Research
   Arlington, Virginia

5. Dr. Ellen Livingston (Code 321OA)
   Office of Naval Research
   Arlington, Virginia

6. Peter H. Dahl
   Applied Physics Laboratory
   University of Washington
   Seattle, Washington